Deepening Understanding of Corium Spreading Involving Melt-Crust Interactions with MPS Method

MPS 法による溶融物—クラスト相互作用を伴う コリウム広がり挙動理解の深化

July 2021

Jubaidah
ジュバイダ

Deepening Understanding of Corium Spreading Involving Melt-Crust Interactions with MPS Method

MPS 法による溶融物―クラスト相互作用を伴う コリウム広がり挙動理解の深化

July 2021

Waseda University
Graduate School of Advanced Science and Engineering
AND
Tokyo City University
Graduate School of Integrative Science and Engineering,

Cooperative Major in Nuclear Energy, Research on Reactor Theory

Jubaidah

ジュバイダ

Abstract

Deepening understanding of molten core material (corium) spreading behavior is important for improving safety evaluations, accident management, accident measures, and light water reactors' design. Numerous corium spreading experiments have shown signs of melt–crust interactions as one of the governing factors to determine corium spreading with limited justifications by numerical simulations. This study aims to deepen understanding of corium spreading through the development of Lagrangian-based Moving Particle Semi-Implicit Method with advanced melt – crust interaction models and analyses of VULCANO VE-U7 and ECOKATS-V1 spreading experiments with the developed MPS method.

Chapter 1 describes the background, the necessity, and the objective of this study. In a postulated severe accident of a light water reactor, the molten core materials (corium) could be released from the reactor pressure vessel (RPV) and spread over the concrete floor of the primary containment vessel (PCV). An accurate understanding of corium spreading is important for evaluating the possibility of the direct corium attack on the PCV boundary wall (for some designs), cool-ability of the corium, and possibility of the subsequent molten core–concrete interaction (MCCI). Some advanced reactor designs adopt core catchers, which are designed to enhance corium spreading. Thus, deepening understanding of corium spreading is necessary to improve safety evaluations, accident managements, accident measures, and designs of light water reactors.

Corium spreading is a free surface flow that involves multiple phenomena. Namely, hydrodynamic flow (involving gravity, inertia, and viscosity) with heat transfer (heat conduction, convection, and radiation) and phase changes (crust formation and re-melting) over a wide temperature range (between liquidus and solidus temperatures), which is finally terminated by sufficient crust formation at the spreading leading-edge. Moreover, experimental observations indicate possible influences of additional complex phenomena, such as influences of concrete substrate decomposition gas bubbles and mechanical fracture of crust on corium spreading behavior. In VULCANO VE-U7, the prototypic corium spreading over the concrete channel with intense outgassing terminated earlier (shorter) than that over the inert ceramic channel. In ECOKATS-V1, some rapid crust formations and breaches were observed, resulting in temporal terminations and restarts of the flow (stop-and-go).

In the meantime, there has been a significant gap between the above-explained understanding from experiments and that understood from numerical simulations. In many cases, the melt flow dynamics were averaged over the melt thickness direction, which limited the capability of such analysis codes (e.g., COREFLOW, MELTSPREAD, THEMA, LAVA) to accurately consider melt–crust interactions. Modeling melt–crust interactions involved in dynamic flow has also been difficult with direct numerical simulation methods, which are based on Eulerian mesh methods (e.g., Volume of Fluid method, Front Tracking method, Level-Set method), because of difficulty in accurately tracking the melt – crust interfaces in dynamic flows.

In contrast, the Moving Particle Semi-Implicit (MPS) method can easily and accurately track melt–crust interfaces in dynamic flows because of its Lagrangian nature. However, applications of MPS methods to deepening corium spreading understanding have been limited to few cases because of poor numerical accuracy and stability in modeling melt–crust interactions. More recently, different techniques have been developed to improve numerical accuracy and stability of MPS method for modeling melt–crust interactions (e.g., elimination of numerical creep for accurate crust modeling, reducing discretization errors by Second-order Corrective Matrix and recovering particle alignment distortions by Particle Shifting to improve numerical stability). Therefore, implementation of these latest techniques, together with further development of MPS method may enable analyses, which greatly deepen our understanding of corium spreading.

Hence, this study aims to deepen the understanding of corium spreading with the improved MPS method. More specifically, the improved MPS method, which has eliminated numerical creep of crust particles and improved accuracy and stability, is applied to VULCANO VE-U7 to investigate possible causes of the shorter spreading length over the concrete substrate channel relative to that over the inert ceramic substrate channel. Furthermore, the stability of the MPS method is further improved to enable simulations of ECOKATS-V1 over a wide range of parameters to test crust formation and fracture conditions to deepen understanding of the stop and go spreading behavior.

Chapter 2 describes the developed MPS method for melt spreading analysis. To consider possible causes of the different spreading over different substrate channels of VULCANO VE-U7, the following modifications and techniques were necessary. Firstly, the basic algorithm of the MPS method was modified to prioritize prompt velocity diffusion by viscosity over prompt velocity correction for assuring incompressibility so that crust formation could be accurately modeled without numerical creeping. Also, Corrective Matrix and Particle Shifting were implemented to reduce discretization error and to improve numerical stability, respectively.

Then, in this study, the new thermal contact resistance model has been proposed and developed to consider different melt–substrate interactions. This model has enabled investigations on possible causes of the different spreading lengths over different substrate channels (concrete VS ceramic) in VULCANO VE-U7. The new model has been developed based on the understanding that the contact between the melt and the substrate is expected to be imperfect due to subscale micro gaps or thin crust layer formation, which cannot be captured in direct simulation due to limited resolution. The newly developed thermal contact resistance model assumes that the heat flux from melt to the interface is equal to the heat flux from the interface to the substrate.

To analyze the stop-and-go spreading of ECOKATS-V1, the crust fracture model was implemented. Moreover, in this study, the new timestep control technique has been developed. In addition to the standard Courant condition, the new timestep control monitors particle number density so that instability due to crust formation and fracture can be avoided efficiently. Then, analyses could be extended over a wide range of parameters.

Chapter 3 is dedicated to the investigation of possible reasons for the different melt spreading lengths over the ceramic and concrete channels of VULCANO VE-U7. The results showed that contact thermal resistance at the melt/crust and the substrate interface did not significantly influence melt spreading, because the crust formation at the leading-edge was more important than crust formation behind the leading-edge (i.e., the melt/crust and the substrate interaction did not have a direct influence on the spreading). Then, possible gas bubble effects on the melt spreading over the concrete channel were investigated. The results showed that the VULCANO VE-U7 spreading could be featured with almost identical spreading of the two channels (ceramic and concrete) until the late phase of the spreading when the spreading of the concrete channel was suddenly hindered relative to that of the concrete channel. Such spreading over the concrete channel could be well explained by the enhanced effective thermal conductivity of the melt (which may be explained in terms of gas bubble agitated internal convection of the melt). The enhancement has the effect of increasing the bulk melt viscosity through the increasement of the solid fraction while the crust development at the melt surface is delayed. As a result, the simulated spreading of the two channels was almost identical until the late phase, when early termination in the concrete channel induced inflow mass to the ceramic channel from the stabilization pool and prolonged the ceramic channel spreading.

Chapter 4 is dedicated to the investigation on the stop-and-go spreading of ECOKATS-V1. The new timestep control with additional consideration of particle number density as a control parameter was confirmed to be effective for employing different crust formation and fracture threshold parameters, namely, Solidification Viscosity Threshold (SVT) and the Crust Fracture Stress Threshold (CFST) of the melt. The former determined the threshold viscosity above which the fluid was regarded as solid (crust). The latter represented the mechanical strength of the crust at the leading edge of the spreading front. However, there remain issues for future studies to further develop the method for more quantitative discussions. In particular, the current 2-D approximation neglects the crust anchoring effect when the resistance of the crust against the bulk melt flow significantly increases as the crust bridges across the channel, between the sidewalls. Moreover, the 2-D approximation requires "complete crust breach" into the plane of the 2-D geometry, whereas in reality, the initial crust fracture develops from a "local weak spot." Due to the 2-D approximation, the current simulation results cannot give any quantitative evaluations for the SVT or CFST. Such quantitative evaluations may be for future study with 3-D analyses.

Chapter 5 summarizes the whole thesis with conclusions. Implementations of the latest techniques to improve numerical accuracy of the MPS method (especially related to modeling melt – crust interaction in dynamic flow) and newly developed thermal contact resistance model and the new timestep control technique have greatly improved numerical accuracy and applicability of the MPS method to a wide range of conditions to investigate corium spreading. The following conclusions can be drawn through analyses of VULCANO VE-U7 and ECOKATS-V1 with the developed MPS method:

- Corium spreading is governed by melt–crust interaction, whose resistance to the flow only

becomes significant when it has developed sufficiently at the leading-edge.

- Melt–substrate interaction does not have a direct influence on corium spreading, but decomposition gas bubbles from the concrete substrate may influence the bulk melt properties and the spreading when the spreading behavior is governed by the bulk melt property change. The bulk melt property change governs the spreading in VULCANO VE-U7 because of the wide solidification range (larger difference between the solidus and the liquidus temperatures). This is the fundamental reason for the difference observed between the ceramic and concrete channel of VULCANO VE-U7.

- The influences of the leading-edge crust formation and fracture are more evident for ECOKATS-V1 than for VULCANO VE-U7, because of the much narrower solidification range of the melt. This is the fundamental reason for the "stop and go" behavior observed in ECOKATS-V1.

- For quantitative discussions, 3-D modeling is necessary to consider the crust anchoring and breaching.

Acknowledgement

In the name of Allah, the most Gracious, the most Merciful.

Table of Contents

List of Figures

List of Tables

Chapter 1 Introduction

1.1. Background

Nuclear safety has been a major concern for the nuclear power industries and the societies, especially post Fukushima nuclear severe accident in 2011. In a hypothesized severe accident of a Light Water Reactor (LWR), the core materials may meltdown and are discharge from the reactor pressure vessel to the reactor containment floor in the form of so-called corium (a mixture of molten core materials). The corium could breach the reactor pressure vessel and spread over the concrete floor of the primary containment vessel (PCV) For some reactors with small containment floor, thermal attack by the corium on PCV liner (see *Figure 1*) may lead to significant release of radioactive materials to the environment (Theofanous, et al., 1993). Moreover, long-term process of the molten core-concrete interaction (MCCI) due to decay heat of the corium may result in extensive erosion of the basemat and threaten containment integrity. Hence, in order to manage the risk of fission product release and manage the reactor containment integrity, a clear understanding of corium spreading behavior is extensively required (Dinh, Konovalikhin, & Sehgal, 2000; Cognet, et al., 2001). Corium spreading knowledge is also essential in designing the advanced core catcher/retention concepts, such as that of the European Pressurized Reactor (EPR) (Fischer, 2004).
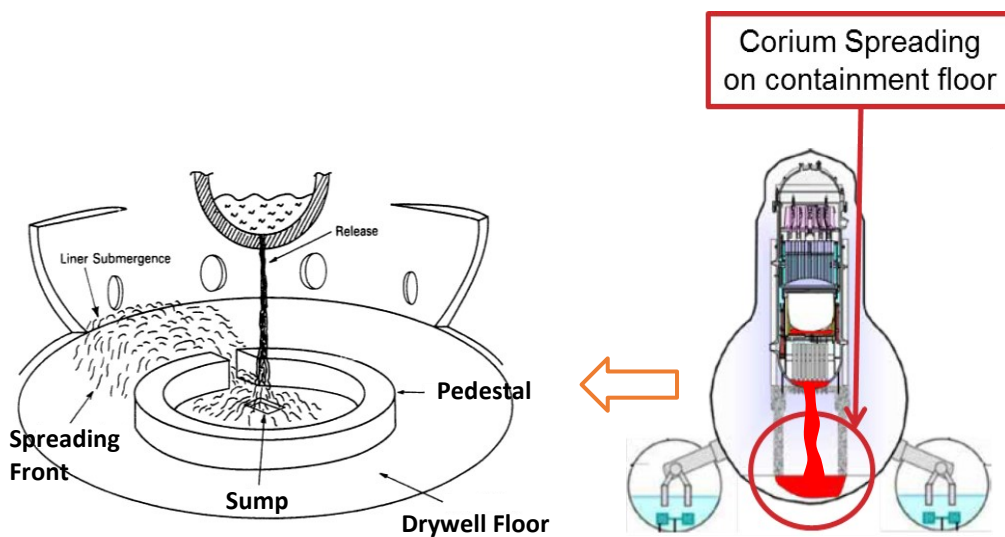
Figure 1 Illustration of corium spreading on PVC liner (Theofanous, et al., 1993)

1.2. Phenomenology of corium spreading on the past studies

Numerous experiments have been conducted with different geometries (1D and 2D spreading channels), different fluids (water, metallic melt, oxidic melt, and prototypic corium), different substrates (inert ceramic, metallic steel, and concrete), and with or without water flooding (Farmer, 2009). Through these experimental studies, together with the accompanied analytical studies, corium spreading is commonly understood as follows: It is a free surface flow, which is governed by complex physical phenomena including the hydrodynamic flow of melt (gravity, inertia, and viscosity) and thermodynamic flow (heat conduction, convection, and radiation) with phase change (crust formation/re-melting) (Dinh, Konovalikhin, & Sehgal, 2000). As observed in some melt spreading experiments (Dinh, Konovalikhin, & Sehgal, 2000; Foit, Large-scale ECOKATS experiments: Spreading of oxide melt on ceramic and concrete surfaces, 2006), interaction of melt with concrete floor involves several additional phenomena, such as massive gas generation, melt eruption caused by the gas bubble burst, and concrete ablation. Compared with spreading over inert substrates, COMAS EU-2b (Steinwarz, Alemberti, Hafner, Alkan, & Fischer, 2001), and 3MDC/S-Ox-1 (Dinh, Konovalikhin, & Sehgal, 2000) experiments indicated that the presence of concrete and sparging gas did not remarkably affect the spreading length. On the contrary, the KATS-12/13 tests (Eigel, Fieg, Massier, Stegmaier, & Schutz, 2000; Eppinger, Fieg, Schutz, & Stegmaier, 2001) and the VULCANO VE-U7 test (Journeau, et al., 2003) demonstrated that intense outgassing over concrete (see *Figure 2*) could significantly restrict the spreading progression. The VULCANO VE-U7 test was a unique spreading experiment, which investigated the potential influence of concrete on corium spreading by a simultaneous inflow of prototypic corium to parallel channels of ceramic and concrete substrates, which were connected by the inlet stabilization pool (Journeau, et al., 2003). The final spreading length of the concrete channel was reported to be about 20 % shorter than that of the ceramic channel (Journeau, et al., 2003). This mechanistic reason for the spreading difference has not been fully understood.

In addition, the so-called "stop-and-go" phenomena were highlighted in FARO L26S test (Tromm & Foit, Dry and wet spreading experiment with prototypical material at the FARO facility and thoretical analysis, 1999) and ECOKATS-V1 test (Foit, Large-scale ECOKATS experiments: Spreading of oxide melt on ceramic and concrete surfaces, 2006) (Alsmeyer, et al., 2004) (Foit, Large-scale ECOKATS experiments: Spreading of oxide melt on ceramic and concrete surfaces, 2006; Alsmeyer, et al., 2004) (see *Figure 3*), in which the low-viscosity melt spreading was temporarily terminated by the formation of crust at the leading edge of the spreading, followed by a restart of the spreading due to what seemed to be crust re-melting or fracture. However, such stop-and-go phenomena have not been well understood.
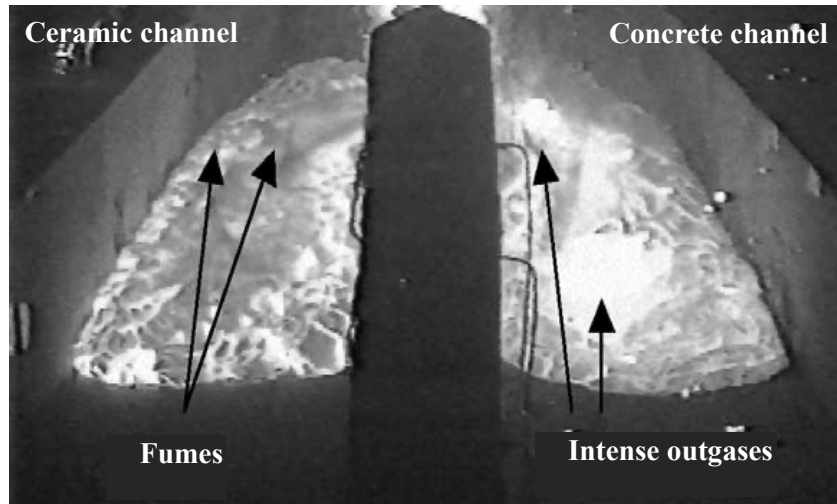
Figure 2 Fumes and melt eruption in VULCANO VE-U7 test (Journeau, Haquet, Spindler, Spengler, & Foit, 2006)
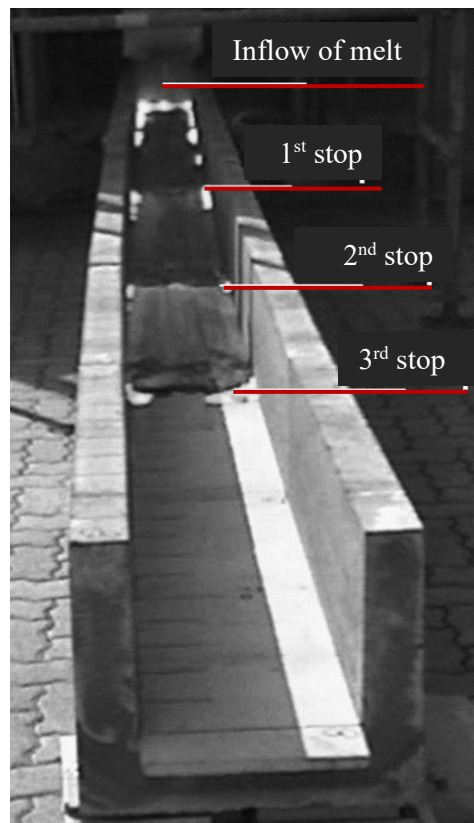
Figure 3 Stop-and-go flow phenomena in ECOKATS-V1 test (Alsmeyer, et al., 2004)

The mechanistic reason for the spreading termination (the "stop") could be explained by a combination of two mechanisms. Firstly, the rapid increase of bulk melt viscosity due to the bulk melt's gradual solidification contributes to the termination of the flow. Secondly, at the same time, crust formation at the leading edge of the spreading may terminate the flow by confining bulk melt, which is

still spreadable. Meanwhile, the crust fracture phenomenon (the "go"), namely the breach of the crust due to either thermal (re-melting) or mechanical failure (stress), which could occur at some weak spots at the interface between the corium leading edge and the substrate, or at the interface between the corium leading edge and the sidewall, as observed in the ECOKATS-V1 experiment (Alsmeyer, et al., 2004). Through these weak spots, the melt may re-flow, resulting in less debris thickness which may increase the debris coolability on the core catcher. However, such stop-and-go phenomena have not been well understood through numerical analyses.

1.3. Past numerical studies on corium spreading

Several code analyses have been developed dedicated to investigating the corium spreading studies numerically. The averaged Eulerian based methods for corium spreading analysis, such as CORFLOW (Wittmaack, 1997), MELTSPREAD (Farmer, Melt Spreading Code Assessement, Modifications, and Applications to the EPR Core Catcher Design, 2009), THEMA (Spindler & Veteau, Status of the Assessment of the Spreading Code THEMA Againts the Corine Experiments, 1998; Spindler, Vetau, Cecco, Montanelli, & Pineau, 2000; Spindler & Veteau, Simulation of spreading wiht solidification: assessment synthesis of THEMA code, 2004; Spindler & Veteau, The simulation of melt spreading with THEMA code Part 1: Model, assessment strategy and assesment againts analytical and nimerical solution, 2006) and LAVA (Spengler, 2004; Allelein, Breest, & Spengler, 2000), have been developed based on the Lubrication hypothesis (Spindler & Veteau, The simulation of melt spreading with THEMA code Part 1: Model, assessment strategy and assesment againts analytical and nimerical solution, 2006). That means the temperature and velocity are averaged in the melt thickness direction. Consequently, only simple crust models with empirical correlations are coupled into these codes which limit the capabilities of these codes to reveal the potential difference between melt spreading over different substrates to some extent. Moreover, capability in addressing "stop-and-go" is limited. Studies with more general-purpose computational fluid dynamics codes are also limited because free surface tracking is complicated and cumbersome for the Eulerian mesh methods with complex interface tracking algorithms (e.g., Volume of Fluid method (Hirt & Nichols, 1981), front tracking (Unverdi & Tryggvason, 1992), level-set (Chang, Hou, Merriman, & Osher, 1996)).

Analytical studies for the apparently shorter spreading distance over concrete substrate relative to the inert substrate have provided some possible reasons. The possible combinations of reasons include: (1) larger radiation heat loss from the melt by the gas bubble sparging (Dinh, Konovalikhin, & Sehgal, 2000; Tromm, Foit, & Magallon, Dry and wet spreading experiment with prototypic material at the FARO facility and theoretical analysis, 2000; Ye, et al., 2013) (2) larger conductive heat loss from the melt to concrete (Spengler, 2004); (3)larger effective viscosity of the melt by the gas bubbles (Dinh, Konovalikhin, & Sehgal, 2000; Foit, Spreading on ceramic and concrete substrate in KATS experiments, 2002; Journeau, Haquet, Spindler, Spengler, & Foit, 2006); (4) uncertainty of inflow melt initial

temperature (Cognet, et al., 2001) (excluding VULCANO VE-U7); (5) different total melt pour mass to the parallel channels (specific for VULCANO VE-U7) (Journeau, et al., 2003). However, there has not been a unanimous understanding of the difference, thereby requiring further investigations.

1.4. MPS method for corium spreading analysis

The Lagrangian based, moving particle semi-implicit (MPS) method (Koshizuka & Oka, Moving Particle Semi-Implicit Method for Fragmentation of Incompressible Fluid, 1996) has been developed for modeling melt-crust interactions in dynamic melt flows. In the MPS method, the melt is discretized with calculation points ("particles") in a Lagrangian manner, which allows for easy free-surface and interface tracking without explicitly calculating the boundaries. The crust formation can be either modeled by fixing the coordinates of the solidified particles (Yasumura, Yamaji, Furuya, Ohishi, & Duan, 2017) or by raising the viscosity of the solidified particles to a sufficiently high value, which effectively terminates the motion of the particle (Duan, Yamaji, & Koshizuka, A novel multiphase MPS algorithm for modeling crust formation by highly viscous fluid for simulating corium spreading, 2019). With these models, the termination mechanism of VULCANO VE-U7 spreading has been successfully demonstrated as crust formation, which develops from the leading edge and confines the bulk melt inside (Yasumura, Yamaji, Furuya, Ohishi, & Duan, 2017)

In the preceding study, the ceramic channel spreading of VULCANO VE-U7 was analyzed with the MPS method to understand the governing mechanism of the spreading and its termination. It was confirmed that viscosity change of the corium was influential to the overall leading-edge progression of the prototypic corium, while termination of the spreading was primarily determined by the immobilization of the leading edge by crust development (Yasumura, Yamaji, Furuya, Ohishi, & Duan, 2017). However, the study was limited in consideration of the melt/crust – substrate interactions as thermal contact resistance at the interface was not considered. The ability to model a thermal contact resistance at the melt / crust - substrate interface is important to consider the potential difference between melt spreading over the inert ceramic substrate and concrete substrate, which undergoes decomposition and melting.

More recently, a crust fracture model has been developed for the MPS method to investigate the stop-and-go phenomena. The model consists of two steps after the crust has developed at the leading edge. The first step is to identify the fracture point by evaluating stress/strain from the relative displacement of solidified particles. The second step is the treatment of the particles to restart the flow. Two different methods have been proposed for the second step and applied to FARO L26S. Namely, relaxing the crust particle viscosity for a given user-defined time (relaxation time) (Uchida, Duan, & Yamaji, 2018), and re-melting the crust particles (Duan et., al., 2018b). However, both treatments have encountered numerical instabilities. Compared with the prototypic corium flow of VULCANO VE-U7, the oxidic melt flow of FARO L26S solidifies over a much narrower temperature range. It leads to

sudden hard crust formation and fracture in a dynamic flow of the low-viscosity melt flow, which is challenging for numerical stability. As a result, the relaxation time had to be tuned to ensure numerical stability, which inevitably affected the flow patterns. The re-melting method only gave stable results for a small number of cases. Thus, the validity of the concept of the crust fracture or quantitative discussions of the spreading involving stop-and-go could not be addressed. In the current MPS method, numerical stability is partly assured by reducing calculation timestep to guarantee Courant stability condition, which usually works fine with single-phase flow. However, the stop-and-go instability may happen at low velocity, and the traditional Courant stability condition may not be efficient for determining appropriate timesteps.

Thus, two experiments, namely VULCANO VE-U7 and ECOKATS V1 have been selected for the development and validation of the MPS methods. The two experiments have been selected to focus on different aspects of corium spreading. VULCANO VE-U7 is suitable for deepening the understanding of melt–substrate interactions on the spreading without the need to consider crust breach. Such assumption may be appropriate not only because it was not observed during the experiment, but the melt used in VULCANO VE-U7 was specifically prepared as the simulant corium for the EPR core catcher. The average composition of the prototypic corium of VULCANO VE-U7 was, in mass percentage, 56% UO_2, 32% ZrO_2, 5% FeO, 2% $CaSiO_3$, 2% SiO_2, 1% Fe, 1% CaO, and 1% Al_2O_3, which represented mixture of corium with the EPR reactor pit sacrificial material which is designed to condition corium for the core catcher (Journeau et al., 2006). According to the literature (Journeau et al., 2006), the initial, liquidus and solidus temperatures of the melt were 2,450 K, 2,623 K and 1,273 K, respectively. Such wide solidification temperature range (1,350 K) implies that crust is gradually formed. Consequently, the melt–crust interaction at the spreading leading edge is more likely to be governed by solidification and remelting rather than mechanical fracturing. In contrast, the appearance of crust fracture was reported by ECOKATS-V1. The composition of simulant oxide melt in ECOKATS-V1 in mass percentage was 41% Al_2O_3, 24% FeO, 19% CaO, and 16% SiO_2. According to the literature (Alsmeyer, et al., 2004), the liquidus and solidus temperatures were 1,822 K and 1,373 K, respectively. Thus, the solidification temperature range of ECOKATS-V1 melt is only 449 K, which is much smaller than that of the melt of VULCANO VE-U7 (1,350 K). The estimated initial melt flow velocity of ECOKATS-V1 is much faster than that of VULCANO VE-U7. Hence, it is sensible to assume no crust fracturing for VULCANO VE-U7, and a significant impact of crust fracturing on spreading for ECOKATS-V1.

1.5. Objectives of current study

Based on the considerations of the above background and issues, this study has two aims. The first aim is to reveal potential difference between melt spreading over inert ceramic channel and concrete channel by referring to VULCANO VE-U7. This study develops a new thermal contact

6

resistance model for MPS method so that influence of different substrates on the heat transfer can be considered. Possible influences of gas bubbles in the concrete channel on the melt spreading are considered with hypothetically increasing the melt viscosity, conductivity, and emissivity. The analyses are first carried out for the ceramic and concrete channel separately, as is done in any other preceding works, to reveal influence of each of these factors. Then, the entire experimental geometry, which models the inlet stabilization pool and the two parallel channels, is modeled to investigate influence of the inflow mass interactions of the two channels for the first time for understanding the potential reason of the different two spreading behaviors of VULCANO VE-U7.

Then, the second aim of this study is to develop the new crust fracture model with a new timestep control method so that the stop-and-go phenomena can be investigated over a wide range of conditions without introducing numerical tuning parameters, such as the relaxation time. ECOKATS-V1 experiment (Alsmeyer, et al., 2004) has been selected for the analyses as the experimental conditions are relatively well defined and summarized in literatures.

1.6. Originality of current study

Investigations on melt–substrate interaction and melt–crust interaction have long been challenging issues for understanding melt spreading behavior. Lagrangian based MPS method has the advantage over other methods for simple and accurate modeling of crust formation and melt crust interactions. However, melt – substrate interactions could not be discussed in detail because of the lack of a thermal contact resistance model. The applicability of the the MPS method was also limited to few cases, where numerical stability was not challenged. These two bottle-neck issues of the MPS method have been significantly hindering further investigations of melt spreading with the MPS method. In this study, these two critical issues of MPS method have been addressed and the improved MPS method has been applied to VULCANO VE-U7 and ECOKATS-V1 experiments to make great advances in the understanding of melt spreading.

More specifically, the new MPS thermal contact resistance model has enabled investigations of VULCANO VE-U7 spreading behavior with consideration of melt – substrate interactions, so that influences of gas bubbles on the melt spreading behavior due to thermal decomposition of the concrete substrate can be discussed for the first time with MPS method. Moreover, the unique stability issue associated with crust formation / fracture in dynamic flow has been successfully identified and resolved by introducing new timestep control using particle number density as the new additional index parameter. This development has greatly expanded the applicability of the MPS method to wide range of melt flow conditions, which is essential to carry out sensitivity analyses of melt spreading involving crust formation and fracture. Thus, the two technological breakthroughs in MPS modeling have now opened new possibility of the use of MPS method to further deepen understanding of melt spreading.

The examples of analyses of VULCANO VE-U7 and ECOKATS-V1 have demonstrated such new frontiers in science and engineering, which is crucial for assuring and improving the safety and reliability of nuclear power.

Chapter 2 MPS Method and Development Models

2.1. MPS method

2.1. 1. Governing equations and basic discretization models

The Moving Particle Semi-implicit (MPS) method (Koshizuka & Oka, 1996) is a Lagrangian mesh-free method for incompressible free surface flow. The basic governing equations for imcompressible multiphase flow are described as conservation of mass, momentum, and energy as follows:

$$\frac{D\rho}{Dt} = -\rho\nabla.\mathbf{u} = 0 \tag{1}$$

$$\frac{D\mathbf{u}}{Dt} = -\frac{1}{\rho}\nabla P + \frac{1}{\rho}\nabla.(\mu\nabla\mathbf{u}) + \mathbf{g} \tag{2}$$

and

$$\frac{DT}{Dt} = \frac{k}{\rho C_P}\nabla^2 T \tag{3}$$

where ρ is density, $\mathbf{u}$ is velocity, P is pressure, μ is dynamic viscosity, $\mathbf{g}$ is gravitational acceleration, T is temperature, k is thermal conductivity and C_P is specific heat capacity.

2.1. 2. Particle Number Density

The Particle Number Density (PND), n, can be calculated based on the weight function as follows:
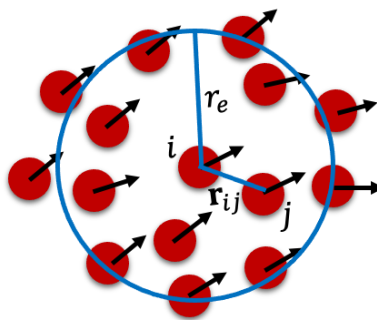
Figure 4 Particle distribution

$$w(r) = \begin{cases} \dfrac{r_e}{r_{ij}} - 1 & (0 \le r_{ij} < r_e) \\ 0 & (r_e \le r_{ij}) \end{cases} \tag{4}$$

Where r_{ij} is the distance between particle i and particle j; $r = |\mathbf{r_j} - \mathbf{r_i}|$; $\mathbf{r}_i$ and $\mathbf{r}_j$ are vector positions of particle i and j; r_e is the effective radius interaction of particle i to its neighboring particles within a vicinity area, in this study $r_e = 3.1 \times l_0$; l_0 is the diameter of particle size. $w(r)$ is the weight function (see Eq. (4)) which was used in the standard MPS method (Koshizuka & Oka, Moving Particle Semi-Implicit Method for Fragmentation of Incompressible Fluid, 1996)

$$w(r) = \begin{cases} \dfrac{r_e}{r} - 1 & 0 \le r < r_e \\ 0 & r_e \le r \end{cases}$$
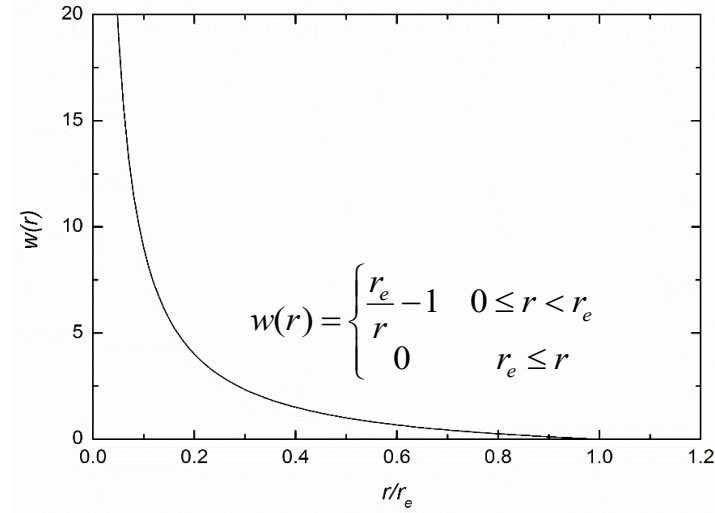
Figure 5 Weight function

$$n_i = \sum_{j \ne i} w(|r_i - r_j|) \tag{5}$$

n_i is the PND of the i-th particle (see Eq. (5)) and n^0 is the initial value of n, which is the same for all the particles and used as the constant reference PND throughout the simulation.

2.1. 3. Particle interaction models

In the MPS method, all terms expressed by differential operators in the above equations are discretized by the particle interaction models based on the weight function, which describes the effect of the neighboring particles to the center particle with respect to their distance. Thus, it is considered that a uniform and regular particle distribution favors the numerical accuracy of the MPS method. The original discretization method namely divergence (Eq. 6), gradient (Eq. 7), and Laplacian (Eq. 8) models are given as follows and illustrated in *Figure 6*:

$$\langle \nabla . \mathbf{u} \rangle = \frac{d}{n^0} \sum_{j \neq i} \frac{(\mathbf{u}_j - \mathbf{u}_i).(\mathbf{r}_j - \mathbf{r}_i)}{|\mathbf{r}_j - \mathbf{r}_i|^2} w(|\mathbf{r}_j - \mathbf{r}_i|) \tag{6}$$

$$\langle \nabla \phi \rangle_i = \frac{d}{n^0} \sum_{j \neq i} \left[\frac{(\phi_j - \phi_i)}{|\mathbf{r}_j - \mathbf{r}_i|^2} (\mathbf{r}_j - \mathbf{r}_i) w(|\mathbf{r}_j - \mathbf{r}_i|) \right] \tag{7}$$

$$\langle \nabla^2 . \phi \rangle_i = \frac{2d}{\lambda n^0} \sum_{j \neq i} [(\phi_j - \phi_i) w(|\mathbf{r}_j - \mathbf{r}_i|)] \tag{8}$$

Where d is the dimension number, and λ is the initial particle distribution, written as:

$$\lambda = \frac{\sum_{j \neq i} r_{ij}^2 w_{ij}}{\sum_{j \neq i} w_{ij}} \tag{9}$$

Difference model   Gradient model   Laplacian model
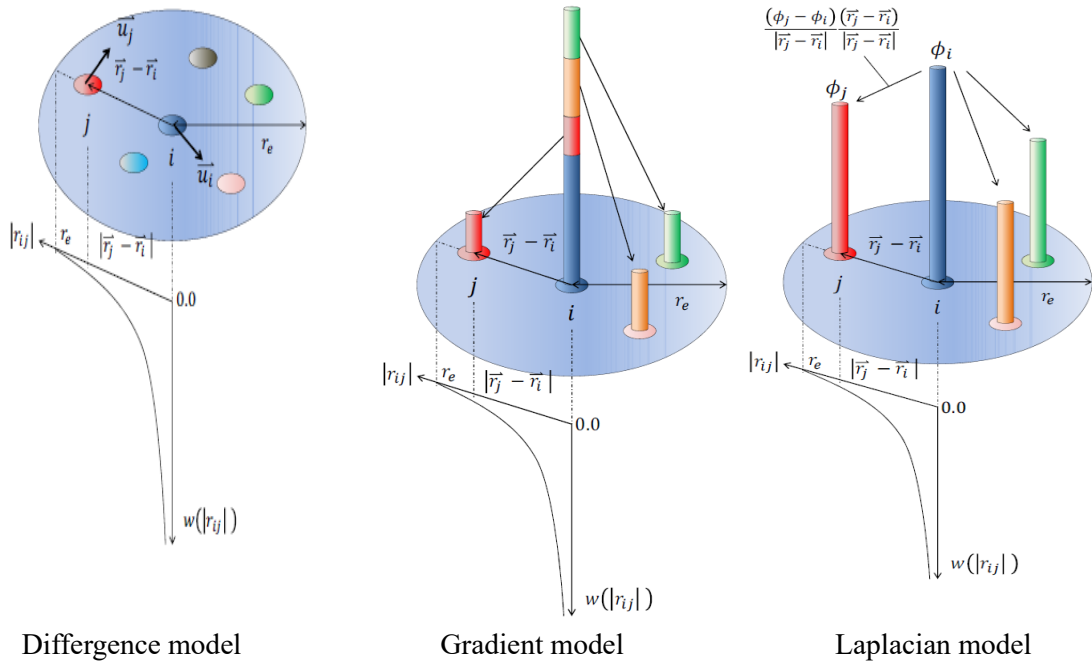
Figure 6 Particle interaction models

2.2. Corrective Matrix

In the incompressible flow, the numerical accuracy of MPS (i.e., divergence, gradient, and Laplacian models) deteriorates if the Particle Number Density (PND) fluctuates from the initial value, especially when particle distribution becomes anisotropic, causing random errors. In this study, to eliminate such anisotropy error and improve numerical accuracy, the original discretization method has

11

been revised by adopting the second-order Taylor series expansion as the fitting function between the particle i and its neighbor particle j, which is expressed with the corrective matrix $\mathbf{C}$ and the relative position vector $\mathbf{P}$ as defined in detail in (Duan, Koshizuka, & Yamaji, An Accurate and Stable Multiphase Moving Particle Semi-Implicit Method Based on Corrective Matrix for All Particle Interaction Models, 2018a) (Duan, Yamaji, & Koshizuka, A Novel Approach for Crust Behaviors in Corium Spreading Based on Multiphase MPS Method, 2018b). Based on this corrective matrix, the gradient model, divergence model, and the Laplacian models are rearranged into the following equations (10), (11), and (12), respectively.

$$\langle \nabla . \mathbf{u} \rangle_i = \frac{1}{n_0} \sum_{j \neq i} \left\{ w_{ij} \frac{\mathbf{u}_j - \mathbf{u}_i}{l_{ij}} \cdot \left(\begin{bmatrix} \mathbf{C}_1 \\ \mathbf{C}_2 \\ \mathbf{C}_3 \end{bmatrix} \mathbf{P} \right) \right\} \tag{10}$$

$$\langle \nabla \phi \rangle_i = \frac{1}{n_0} \sum_{j \neq i} \left\{ w_{ij} \frac{\phi_j - \phi_i}{l_{ij}} \left(\begin{bmatrix} \mathbf{C}_1 \\ \mathbf{C}_2 \\ \mathbf{C}_3 \end{bmatrix} \mathbf{P} \right) \right\} \tag{11}$$

$$\langle \nabla^2 \phi \rangle_i = \frac{2}{n_0} \sum_{j \neq i} \left\{ w_{ij} \left(\phi_j - \phi_i \right) \frac{[\mathbf{C}_4 + \mathbf{C}_5 + \mathbf{C}_6]\mathbf{P}}{l_0 l_{ij}} \right\} \tag{12}$$

$$\mathbf{C}_i^{-1} = \frac{d}{n_0} \begin{pmatrix} \sum_{j \neq i} \dfrac{x_{ij}^2}{r_{ij}^2} w_{ij} & \sum_{j \neq i} \dfrac{x_{ij} y_{ij}}{r_{ij}^2} w_{ij} \\ \sum_{j \neq i} \dfrac{y_{ij} x_{ij}}{r_{ij}^2} w_{ij} & \sum_{j \neq i} \dfrac{y_{ij}^2}{r_{ij}^2} w_{ij} \end{pmatrix} \tag{13}$$

where ϕ is the scalar variable; $\mathbf{C}$ is the corrective matrix; $\mathbf{C}_1$, $\mathbf{C}_2$ and $\mathbf{C}_3$ are the first, second and third rows of $\mathbf{C}$, respectively; $\mathbf{P}$ is column vector, n_0 is the initial particle number density; l_{ij} is distance between particle i and particle j; l_0 is diameter of particle size, and $w(r)$ is the weight function. The weight function and particle number density are defined as in standard MPS method (Koshizuka & Oka, 1996). Furthermore, the stabilizing methods as adopted in the preceding study (Duan, Koshizuka, & Yamaji, An Accurate and Stable Multiphase Moving Particle Semi-Implicit Method Based on Corrective Matrix for All Particle Interaction Models, 2018a) has also been utilized in this study to attain improved numerical stability. These improvements have been incorporated in the general MPS code being developed at Waseda University, which is not only applied to corium spreading applications, but to other applications, where improvement in numerical accuracy may be more important (e.g., analysis of vessel wall ablation with natural circulation of melt pool).

2.3. Developed models

In the past melt spreading analyses with the MPS method, perfect heat conduction between the melt particle and the substrate particle was assumed for the cases with different particle sizes ranging from 3 mm to 10 mm (Yasumura, Yamaji, Furuya, Ohishi, & Duan, 2017). In reality, there may be microscale phenomena (e.g., microscale flow, micro gap), which may promote or suppress heat transfer between the melt and the substrate, which cannot be captured with such large particle sizes. For VULCANO VE-U7, it was reported that there could be large thermal contact resistance (>3E-3 Km^2/W) (Journeau, et al., 2003). However, the influence of such thermal contact resistance could not be considered in the past studies with the MPS method, which limited further deepening understanding of the spreading. Therefore, in this study, a new thermal contact resistance model has been developed. The thermal conduction model used in MPS method has been modified to consider thermal contact resistance as described in the following section.

2.3.1. Melt-substrate thermal resistance model

The heat conduction is calculated by discretizing the Eq. (3) with Eq.(12), resulting in the following discretized form:

$$T_i^{k+i} = T_i^k + \frac{\Delta t}{\rho C_P} \frac{2}{n_0} \sum_{j \neq i} \left\{ k_{ij}(T_j^k - T_i^k) w_{ij} \frac{[\mathbf{C_4 + C_5 + C_6}]\mathbf{P}}{l_0 r_{ij}} \right\} \tag{14}$$

where k_{ij} is the harmonic mean effective conductivity between two particles:

$$k_{ij} = \frac{2k_i k_j}{k_i + k_j} \tag{15}$$

In the previous MPS spreading analyses, heat transfer between solid–liquid interface is approximated by an ideal heat conduction (Yasumura, Yamaji, Furuya, Ohishi, & Duan, 2017; Matsuura & Oka, 2013) of particles with limited resolution. However, the temperature profiles inside the substrate in the previous simulations (Yasumura, Yamaji, Furuya, Ohishi, & Duan, 2017) were obviously overestimated. The main reason is probably that the contacting surfaces between melt and substrate are imperfect. In other words, some subscale micros gaps exist between two real contacting surfaces, as shown in *Figure 7*.
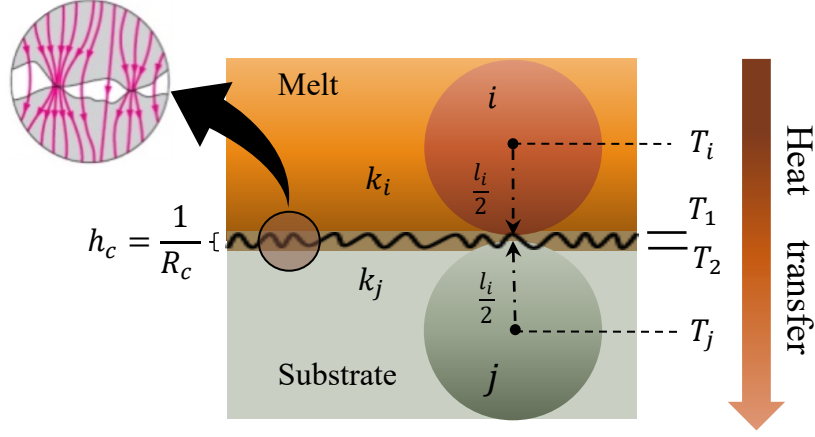
Figure 7 Sketch for the melt-substrate thermal resistance model in MPS

In this study, a new melt-substrate heat transfer model is proposed for MPS to consider the thermal contact resistance between melt and substrate. Based on the Fourier's law of conduction, the heat flux from corium to the gap, heat flux between the gaps, and heat flux from the gap to substrates, should equal each other, as expressed in Eqs. (16) and (17), respectively:

$$-k_i \frac{(T_1 - T_i)}{\frac{1}{2}l_i} = h_c(T_1 - T_2) \tag{16}$$

$$h_c(T_1 - T_2) = -k_j \frac{(T_j - T_2)}{\frac{1}{2}l_j} \tag{17}$$

where k_i is the conductivity of corium particle i, k_j is the conductivity of substrate particle j, h_c is heat contact conductance, l_i and l_j are the diameter of particle i and particle j, respectively. T_1 is the interface temperature of the gap on the melt side, and T_2 is that of the substrate side. These variables are also shown in *Figure 7*. Assuming a heat flux q, Eqs. (16) and (17) can be rearranged as follows:

$$k_i \frac{(T_i - T_1)}{\frac{1}{2}l_i} = h_c(T_1 - T_2) = k_j \frac{(T_2 - T_j)}{\frac{1}{2}l_j} = q \tag{18}$$

From Eq. (18), the temperature differences can be derived as follows:

$$\begin{cases} T_i - T_1 = \dfrac{l_i}{2k_i}q \\ T_1 - T_2 = \dfrac{1}{h_c}q \\ T_2 - T_j = \dfrac{l_j}{2k_j}q \end{cases} \tag{19}$$

By eliminating T_1 and T_2 in Eq. (19), the heat flux can be calculated from:

14

$$q = \frac{T_i - T_j}{\left(\frac{l_i}{2k_i} + \frac{1}{h_c} + \frac{l_j}{2k_j}\right)} \tag{20}$$

In terms of particles i and j, the heat flux at the interface can also be defined based on the effective interparticle thermal conductivity $(k_{ij,interface})$ as follows:

$$q = \frac{k_{ij,interface}}{\frac{1}{2}l_i + \frac{1}{2}l_j}(T_i - T_j) \tag{21}$$

Substitution of the Eq. (20) to the Eq. (21) results in the new interparticle conductivity:

$$k_{ij,interface} = \frac{2}{\left[\frac{1}{k_i} + \frac{1}{k_j} + \frac{2R_c}{l_0}\right]} \tag{22}$$

where l_0 is diameter of particle size ($l_0=l_i=l_j$), and R_c is the thermal contact resistance ($R_c = 1/h_c$). It is noted that (1) the above derived $k_{ij,interface}$ is only adopted for heat transfer between the melt/crust and substrate particles identified based on Neumann Boundary condition as shown in Figure 8, while (2) the original interparticle conductivity k_{ij} (Yasumura, Yamaji, Furuya, Ohishi, & Duan, 2017; Matsuura & Oka, 2013; Duan, Yamaji, & Koshizuka, A novel multiphase MPS algorithm for modeling crust formation by highly viscous fluid for simulating corium spreading, 2019) is still utilized for the melt-melt or substrate-substrate heat conduction.
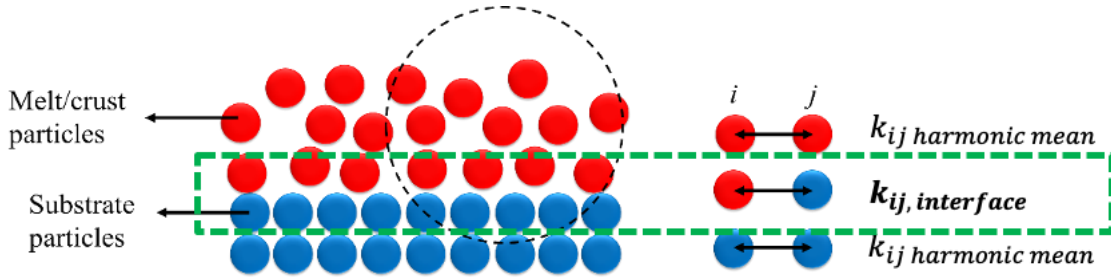
Figure 8 Illustration of melt/crust-substrate interaction

2.3.2. Free surface detection

While heat conduction and convection can be well considered with the basic discretization described in Section 2.1., radiation heat transfer must be modeled separately. This study adopts a simple method as also adopted by the preceding studies (Li, 2015) (Masumura, Oka, Yamaji, & Furuya, 2015). Firstly, the free-surface particles are detected from the decrease of PND, n, (Koshizuka & Oka, Moving Particle Semi-Implicit Method for Fragmentation of Incompressible Fluid, 1996) and the number of neighbor particles, N, (Tanaka & Masunaga, 2010) as shown in Eq. (23) and Eq. (24), respectively.

$$n_i^* < \beta n^0 \tag{23}$$

$$N_i^* < \beta' N^0 \tag{24}$$

15

where N_i^* is the number of a neighbor particle of the i-th particle; N^0 is the constant reference value of N (defined in the same manner as to n); β and $β'$ are the threshold parameters for the number density and the number of neighbor particles, with 0.95 and 0.85 chosen for the current study, respectively. If the Eq. (23) and Eq. (24) are satisfied, then further scan will be employed with the following conditions (Tamai & Koshizuka, 2014):

$$\|\mathbf{r}_j - \mathbf{r}_i\| \geq \sqrt{2}l_0$$
$$\|(\mathbf{r}_i + l_0\mathbf{n}) - \mathbf{r}_j\| < l_0 \tag{25}$$

or

$$\begin{cases} \|\mathbf{r}_j - \mathbf{r}_i\| < \sqrt{2}l_0 \\ \dfrac{\mathbf{r}_j - \mathbf{r}_i}{\|\mathbf{r}_j - \mathbf{r}_i\|} \cdot \mathbf{n} > \dfrac{1}{\sqrt{2}} \end{cases} \tag{26}$$

where l_0 is the diameter of particle size, $\mathbf{r}_i$ is the coordinate position of particle i, $\mathbf{r}_j$ is the coordinate position of particle j, and $\mathbf{n}$ is the unit normal of free surface, which is calculated from:

$$\mathbf{n} = \frac{\mathbf{N}}{\|\mathbf{N}\|}, \qquad \mathbf{N} = \frac{1}{n_i} \sum_{j \neq i} \left\{ \frac{\mathbf{r}_j - \mathbf{r}_i}{\|\mathbf{r}_j - \mathbf{r}_i\|} w(\|\mathbf{r}_j - \mathbf{r}_i\|) \right\} \tag{27}$$

Only particles satisfying the above conditions (25) or (26) will be judged as free-surface particles. Otherwise, the particles will be noted as internal liquid particles.

2.3.3. Radiation heat transfer model

Then, the radiation heat transfer (Q_e) at the free surface is evaluated as follows (Takahashi, Duan, Furuya, & Yamaji, 2019):

$$Q_e = \varepsilon_A \sigma_{Stef} A_i T_i^4 \tag{28}$$

where,

$$A_i = \left(1 - \frac{n_i}{n^0}\right) 2l_0{}^2 \tag{29}$$

where ε_A is the radiation emissivity, σ_{Stef} is the Stefan-Boltzmann constant, A_i is the surface area of the free-surface particles, T_i is the temperature of target particle i, and l_0 is the particle size.

2.3.4. Liquid-solid phase change model

The liquid-solid phase change model was developed by simply differing the liquid particles, solid particles, and mixture particle based on their temperature as a function of enthalpy (Kawahara & Oka, 2012), as illustrated in *Figure 9*, and expressed in Eq. (30) and Eq. (31).
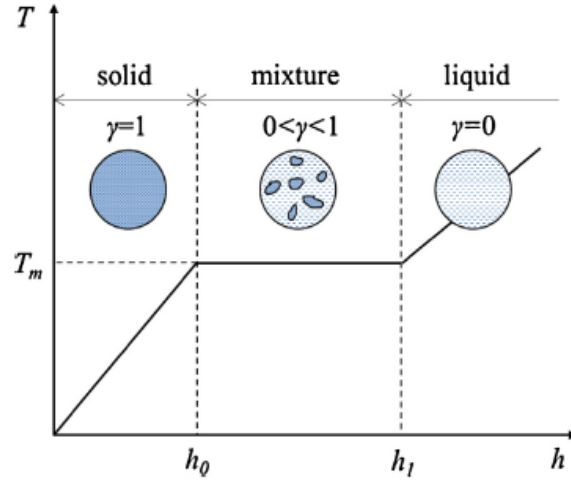
Figure 9 Liquid-solid phase change

$$(T) = \begin{cases} T_m + \dfrac{h - h_0}{\rho C_{ps}} & (h < h_0) \\[2mm] T_m & (h_0 \leq h \leq h_l) \\[2mm] T_m + \dfrac{h - h_l}{\rho C_{ps}} & (h_l < h) \end{cases} \tag{30}$$

$$\gamma(T) = \begin{cases} 1 & (h < h_0) \\[2mm] \dfrac{h_l - h}{h_l - h_0} & (h_0 \leq h \leq h_l) \\[2mm] 0 & (h_l < h) \end{cases} \tag{31}$$

Where $\gamma(T)$ is the solid fraction of the melt; h is the specific enthalpy of the corium; h_0 and h_l refer to the enthalpy of the corium at the solidus and liquidus temperature, respectively, and T_m is melting temperature.

2.3.5. Crust formation model

In the original MPS algorithm, a temporary estimate of the particle velocity is evaluated with consideration of velocity diffusion by the viscosity, which is then corrected by the pressure term before proceeding to the next time step. In this manner, incompressibility of the fluid is guaranteed exactly within any time step, while velocity diffusion by viscosity is delayed to the next time step, because the velocity correction by the pressure term does not consider viscosity. This causes the so called "numerical creep" when the particle velocity approaches zero. For simulating termination of corium spreading, immobilization of crust needs to be accurately modeled. For such purpose, two methodologies have been developed. In one method (crust adhesion model), the original MPS algorithm is used, and crust is immobilized by fixing crust particle coordinate in space (Yasumura, Yamaji, Furuya, Ohishi, & Duan, 2017) as illustrated in *Figure 10*. In another method, the MPS algorithm is revised, and the viscosity term is calculated after the pressure term (Duan, Yamaji, & Koshizuka, A novel multiphase MPS algorithm for modeling crust formation by highly viscous fluid for simulating corium spreading, 2019), as shown in *Figure 11*. The former guarantees exact incompressibility but may be more susceptible to numerical instability and the latter is vice versa. In this study, the latter method is used with the revised MPS algorithm as the code is being developed for more generalized application of simulating melt behavior, which tends to encounter more numerical stability issue than incompressibility issue.
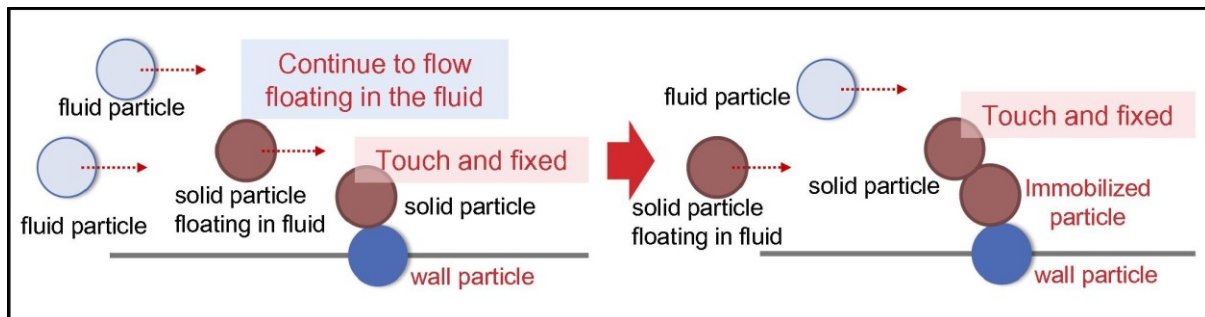
Figure 10 Crust adhesion model in MPS method (Yasumura, Yamaji, Furuya, Ohishi, & Duan, 2017)

Suitable for low viscosity fluid

Explicitly calculate gravity term: $\Delta\mathbf{u}_g$

↓

Implicitly calculate viscosity term: $\Delta\mathbf{u}_v$

↓

$\mathbf{u}^* = \mathbf{u}^k + \Delta\mathbf{u}_g + \Delta\mathbf{u}_v$
$\mathbf{r}^* = \mathbf{r}^k + \mathbf{u}^* \cdot \Delta t$

↓

Implicitly calculate pressure term: $\Delta\mathbf{u}_p$

↓

$\mathbf{u}^{k+1} = \mathbf{u}^* + \Delta\mathbf{u}_p$
$\mathbf{r}^{k+1} = \mathbf{r}^* + \Delta\mathbf{u}_p \cdot \Delta t$

Adhesion MPS algorithm

Suitable for high viscosity fluid

Explicitly calculate gravity term: $\Delta\mathbf{u}_g$

↓

$\mathbf{u}^* = \mathbf{u}^k + \Delta\mathbf{u}_g$
$\mathbf{r}^* = \mathbf{r}^k + \mathbf{u}^* \cdot \Delta t$

↓

Implicitly calculate pressure term: $\Delta\mathbf{u}_p$

↓

Implicitly calculate viscosity term: $\Delta\mathbf{u}_v$

↓

$\mathbf{u}^{k+1} = \mathbf{u}^* + \Delta\mathbf{u}_p + \Delta\mathbf{u}_v$
$\mathbf{r}^{k+1} = \mathbf{r}^* + (\Delta\mathbf{u}_p + \Delta\mathbf{u}_v) \cdot \Delta t$

Solidification MPS algorithm

$\nu = 10000.0 \ \mathrm{m^2/s}$

Figure 11 Highly viscous fluid (HVF) model in MPS method (Duan, Yamaji, & Koshizuka, A novel multiphase MPS algorithm for modeling crust formation by highly viscous fluid for simulating corium spreading, 2019)

Phase change between liquid and solid is one of the main features in corium spreading. According to various studies in the field of rheology, liquid gradually changes its phase to solid between the liquidus and the solidus temperature through the phase change region (mushy zone). In the field of fluid dynamics, the mushy zone is commonly regarded as fluid with volumetric solid fraction, which indicates the volumetric fraction of solid contained in the mixture. The solid fraction needs to be evaluated with, for example, thermo-dynamic calculations. Then, the Navier-Stokes' equation (Eq. (2) is solved with viscosity, which is usually given as a function of the solid fraction of the mixture. In the Lagrangian-based MPS method, there is no convective term. Hence, the solid fraction can be directly assigned to particles, which constitute the melt. Therefore, mechanistic and accurate modeling of solidification and re-melting is possible.

Similarly, solidification, in the field of fluid dynamics, is often regarded as immobilization of the melt. In this study, when the solid fraction of a particle reaches a user defined immobilization solid fraction, the solidified particle is practically immobilized by arbitrarily increasing the viscosity by a sufficiently large factor (e.g., 100 times). The immobilization solid fraction has to be determined by some other methods and may be regarded as one of the parameters for sensitivity analyses in this study. From hereafter, the immobilized particles are defined as "crust" particles.

The crust formation model of this study is the same as those used in the preceding studies (Uchida, Duan, & Yamaji, 2018) (Duan, Yamaji, & Koshizuka, A Novel Approach for Crust Behaviors in Corium Spreading Based on Multiphase MPS Method, 2018b). Solid fraction of the melt is assumed to linearly increase from 0 to 1 as its enthalpy is reduced from the liquidus temperature to the solidus

temperature. Then, the viscosity of the melt in the "mushy zone" between the liquidus and the solidus temperature is evaluated as a function of the solid fraction with empirical correlations as described in Section 3.2. To represent "crust", viscosity of the melt is increased by a sufficiently large factor when solid fraction of the particle reaches a user-defined solidification solid fraction threshold. From hereafter, the solid particles are defined as "crust" particles.

2.3.6. Crust fracture model

The crust fracture model consists of two parts. Namely, detection of the fracture particles and treatment of the fracture (Duan, Yamaji, & Koshizuka, A Novel Approach for Crust Behaviors in Corium Spreading Based on Multiphase MPS Method, 2018b). Firstly, the fracture particles are identified based on the strain rate integral as follows:

$$S_{\alpha\beta} = \int_{-\infty}^{t} \varepsilon_{\alpha\beta} W(t - t')dt' \tag{32}$$

With

$$\varepsilon_{\alpha\beta} = \frac{1}{2}\left(\frac{\partial u_\alpha}{\partial u_\beta} + \frac{\partial u_\beta}{\partial u_\alpha}\right) \tag{33}$$

and

$$W(t - t') = \frac{1}{T}exp\left(-\frac{t - t'}{T}\right) \tag{34}$$

where ε is the strain rate tensor, t is the current moment, t' is the historical moment, and T is the relaxation time for historical memory.

Then, the stress tensor is calculated from the product of viscosity and strain rate. Afterward, the fracture particle is detected from the von-Mises stress criterion as written in Eq. (35). If the σ_{Mises} is larger than the critical value, namely Crust Fracture Stress Threshold, a fractured particle or a crack is detected as illustrated in *Figure 12a*.

$$\sigma_{Mises}^2 = 0.5\mu_{SVT}[(\varepsilon_{11} - \varepsilon_{22})^2 + (\varepsilon_{22} - \varepsilon_{33})^2 + (\varepsilon_{33} - \varepsilon_{11})^2 + 6(\varepsilon_{12}^2 + \varepsilon_{23}^2 + \varepsilon_{31}^2)] \tag{35}$$

where μ_{SVT} is the Solidification Viscosity Threshold (SVT) of the melt.

The so-called Mises stress in this study is just a variable similar to the Mises stress for elastic solid. In Eq. (35), the strain rate used is the averaged strain rate in Eq. (32) rather than the original one in Eq. (33). The relaxation time, T, helps to consider the effects of the accumulative/historic strain rates. The influence of the relaxation time was discussed in (Duan, Yamaji, & Koshizuka, A Novel Approach for Crust Behaviors in Corium Spreading Based on Multiphase MPS Method, 2018b). Because the high-

viscosity fluid is used to represent the solid, adjustments have to be made for the Von Mises criterion.

When the fractured particles are detected (*Figure 12a*), the crust fracture model is activated with the re-melting method (Duan, Yamaji, & Koshizuka, A Novel Approach for Crust Behaviors in Corium Spreading Based on Multiphase MPS Method, 2018b), in which the temperature of the fractured crust particles was set back to a high temperature (e.g., the inlet temperature of the corium) (see *Figure 12b*), in order to form an opening on the crust and result in crust break-up. It is obvious that the critical value of the σ_{Mises} (i.e., crust fracture stress threshold) is important in determining the crust fracture behavior.

(a) Detection of fractured particle   (b) Treatment of fractured particle
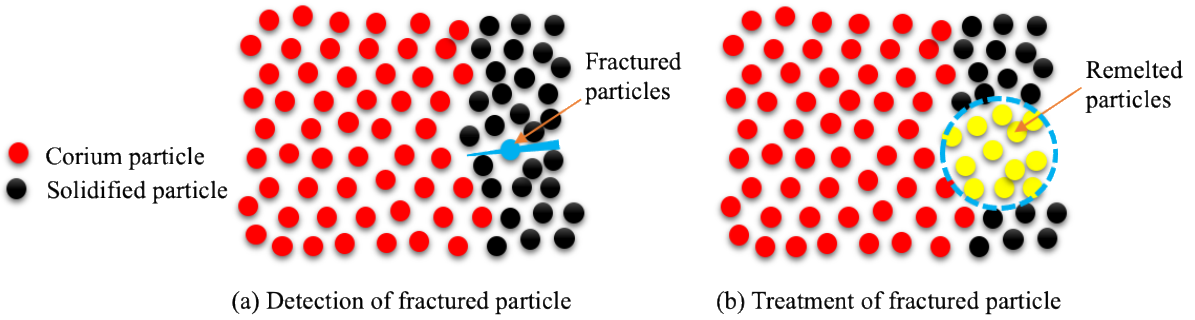
Figure 12 Crust fracture model in MPS method (Duan, Yamaji, & Koshizuka, A Novel Approach for Crust Behaviors in Corium Spreading Based on Multiphase MPS Method, 2018b)

2.4. Particle Shifting

The Particle Shifting (PS) technique (Xu, Stansby, & Laurence, 2009) is used to suppress the particle clustering, and that could occur in the fluid by artificially relocating the fluid particles from the particle-dense region to the particle-dilute region with a position vector defined in Eq. (36). The optimized PS (OPS) (Khayyer, Gotoh, & Shimizu, 2017) technique and the conservative pressure gradient model (Duan, Chen, Koshizuka, & Xiang, 2017) are applied to the free surface particles simultaneously to produce appropriate surface tangent and normal adjustments, respectively.

$$\delta \boldsymbol{r}_i = -\frac{l_0 \Delta r_i}{n_0} \sum_{j \neq i} \frac{w_{ij}}{r_{ij}^2} \boldsymbol{r}_{ij} \tag{36}$$

where Δr_i is the distance coefficient controlling the amplitude of position shifting. The PS treatment for the surface particles is different from that of the internal particles, as described in the works by Duan et al (2018a).

2.5. New timestep control

In the past melt spreading studies with MPS method, low viscous melt spreading with sharp crust formation and crust breach could only be analyzed for a limited number of cases, which gave numerically stable results (Uchida et al., 2018). For other cases, the simulations were often unstable, and it has been an issue to stabilize such simulation.

It is well known that for a fluid dynamics analysis, information being transferred through the calculation domain should travel much faster than the actual phenomena being transferred. In another word, the timestep should be fine enough compared with the timescale of phenomena being transferred. Otherwise, the simulation would become unstable or inaccurate. Hence, typically, the Courant number condition is given as an index to consider appropriate timestep control. However, due to the nature of MPS simulation, it may not be sufficient to give appropriate timestep control when the focus of the simulation is about the termination of melt flow due to solidification.

As described in Chapter 2, the MPS method requires incompressibility to guarantee numerical accuracy and stability. However, assuring incompressibility may not always be well guaranteed especially, when there are solidifications of particles in dynamic flows. When a particle solidifies, its viscosity would suddenly increase by a large factor and the particle may stop its motion while its surrounding particles may still continue to flow as liquid particles. Then, particle alignments and particle number density (i.e., incompressibility) may not be well guaranteed around the solidified particle. For such numerical instability, the Courant number condition may not be an appropriate index to give timestep control, because the solidifying particle may not be travelling at high speed. Hence, in this study, the particle number density is proposed as a new index to avoid such numerical instability. Then, the modified MPS method is expected to be applicable to a wide range of flow conditions, which is essential to conduct sensitivity analyses to deepen understanding of corium spreading. The details are given as follows.

In the semi-implicit algorithm, a sufficiently small timestep is necessary to guarantee the simulation stability. Traditionally, the timestep (Δt) is controlled by the Courant number of a flow velocity as written as follows:

$$\Delta t = \frac{l_0 C_i}{u_i} \tag{37}$$

$$C_i < 0.2 \tag{38}$$

where C_i, u_i, Δt, l_0 are Courant number of flow velocity, maximum flow velocity, timestep, and the space between two adjacent particles, respectively.

However, when instability is not from the locally high velocity, this Courant stability condition could not help improving the stability because it is mainly intended for assuring transferring information faster than the physical phenomenon of interest. Thus, in this paper, a new technique of timestep control

is proposed by applying a PND control as an addition to the Courant number control. First of all, the timestep is calculated based on the Courant number. Then, based on the relationship of the maximum PND calculated for each timestep and the threshold PND $n_{condition}$ set for the simulation, the PND control is judged to be applied or not, resulting in the following possible steps as the flow shown in *Figure 13*:

(1) When the maximum PND is below the threshold (i.e. $n_{condition} = 3.0 \times n^0$), the timestep calculated by the Courant condition $\Delta t_{courant}$ is applied, with the maximum timestep being 0.001 s.

(2) When the maximum PND is above the threshold (i.e. $n_{condition} = 3.0 \times n^0$), the PND condition is applied. The timestep Δt by PND control will be divided into the following scenarios.

    a. If Δt is less than the minimum timestep Δt_{lim} set in the simulation, Δt will be used.

    b. If Δt is larger than Δt_{lim}, but 2/3 of the timestep Δt is smaller than Δt_{lim}, then Δt_{lim} will be used.

    c. If 2/3 of the timestep Δt is judged to be larger than Δt_{lim}, then $\frac{2}{3}\Delta t$ will be used as the timestep.
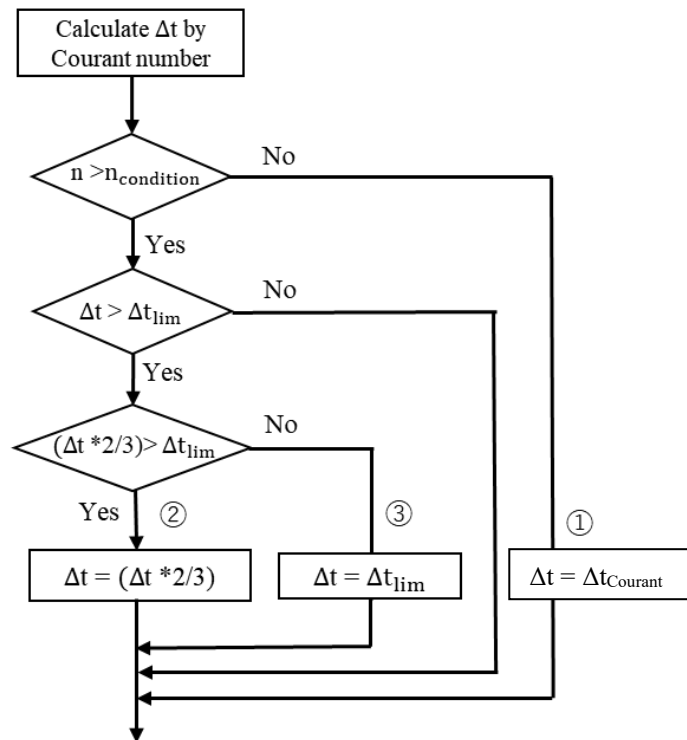
Figure 13 Flow chart of new timestep control

Chapter 3 Simulations of VULCANO VE-U7 test with MPS Method

3.1. Test description of VULCANO VE-U7

The VULCANO VE-U7 (VE-U7) experiment (Journeau, et al., 2003; Foit, Large-scale ECOKATS experiments: Spreading of oxide melt on ceramic and concrete surfaces, 2006) was one of the VULCANO experimental series using prototypic corium conducted by French Atomic Energy Commission (CEA) Cadarache as part of R&D program for understanding the severe accidents. The VULCANO VE-U7 is a unique spreading experiment, which investigated the potential influence of concrete on corium spreading by simultaneous inflow of prototypic corium to parallel channels of ceramic and concrete substrates, which were connected by the inlet stabilization pool (Journeau, et al., 2003). The final spreading length of the concrete channel was reported to be about 20 % shorter than that of the ceramic channel (Journeau, et al., 2003).

The VE-U7 experiment was designed for mastering the corium spreading over reactive (concrete) substrate compared to over inert (dense zirconia ceramic) substrate as a reference. The experimental setup of VE-U7 was described in detail in (Journeau, Haquet, Spindler, Spengler, & Foit, 2006). In brief, the flow geometry was consisted of the stabilization pool and the spreading plane section. The spreading plane section was a 19 °angular sector consisted of two parallel channels of ceramic and concrete substrates as shown in *Figure 14*. The initial temperature was measured at the spreading entrance at 2750 K, and the test section were and about 300 K. A total of 40.8 kg of the melt was poured into the stabilization pool, which had depth of 5.0 mm below the test sections. A weighing scale mounted to the spreading channels showed the melt spread equally on both channels up to about the first 8s (see *Figure 15*), but the final total masses spreading over the ceramic and concrete channels were 14.0 and 12.6 kg, respectively.
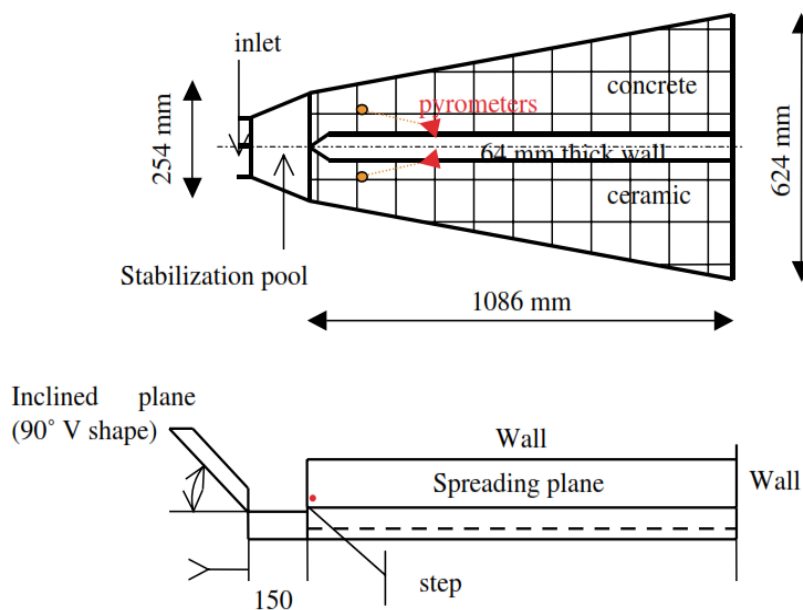
Figure 14 Flow geometry of VE-U7 test (Journeau, C., et. al., 2006)
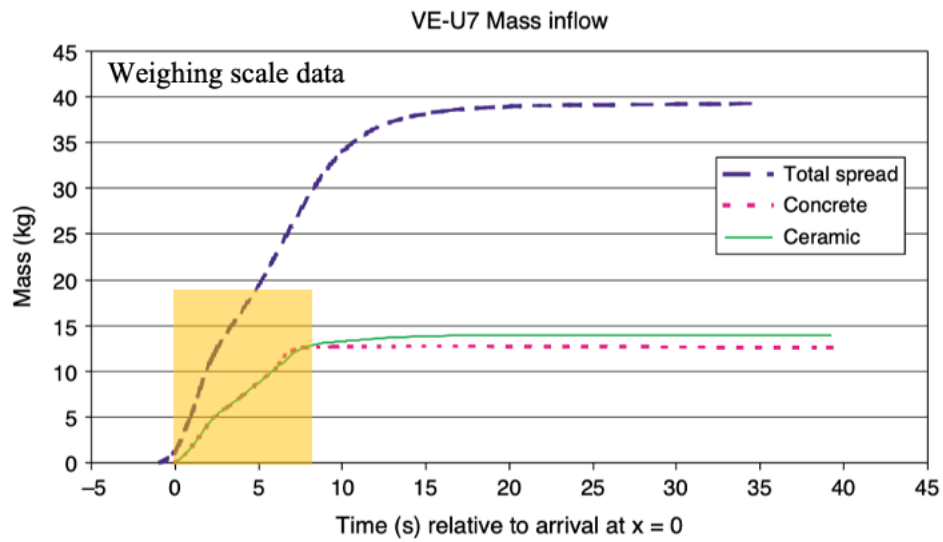
Figure 15 *VE-U7 mass inflow on the test section (Journeau, Haquet, Spindler, Spengler, & Foit, 2006)*
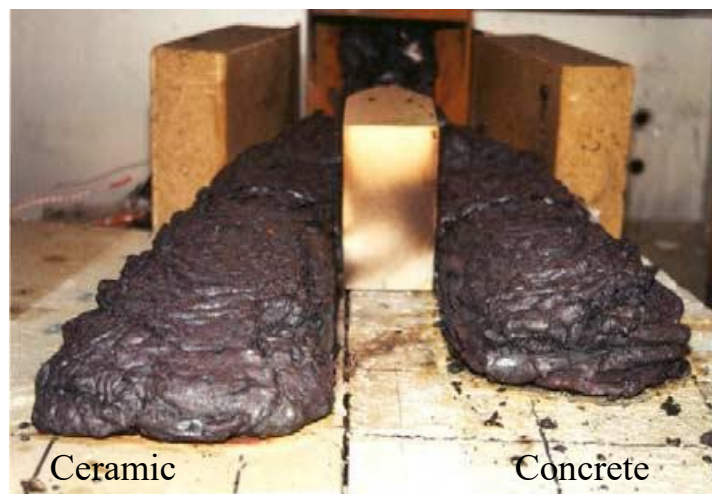
Figure 16 VULCANO VE-U7 spreading result (Journeau, Haquet, Spindler, Spengler, & Foit, 2006)
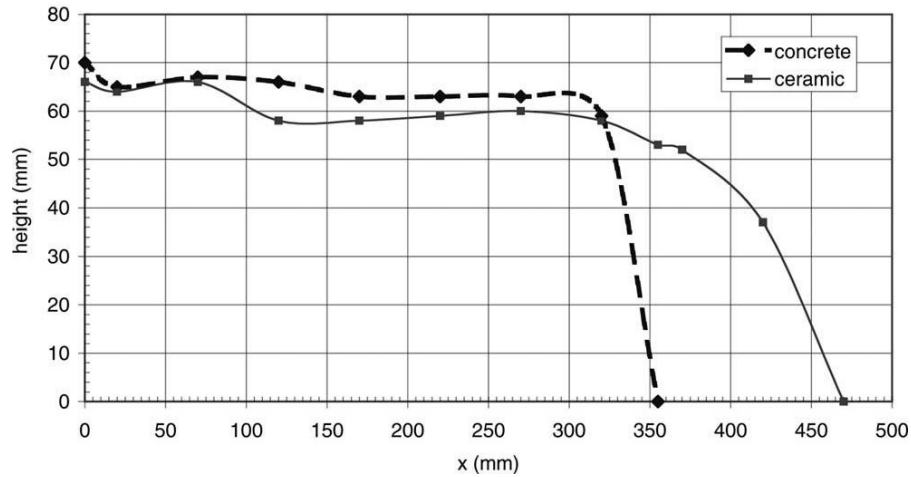
Figure 17 VE-U7: Average spreading heights (Journeau, Haquet, Spindler, Spengler, & Foit, 2006)

The post-mortem result showed that the spreading length over the concrete channel is about 20% shorter than that on the ceramic channel (see *Figure 16* and *Figure 17*). The spreading leading edge over the channel was more cliff than the ceramic one. Moreover, a high porosity in both spreading channel as reported in (Journeau, et al., 2003) (see *Figure 18*) with a few millimeters' ablations on the concrete floor (Journeau, Haquet, Spindler, Spengler, & Foit, 2006).
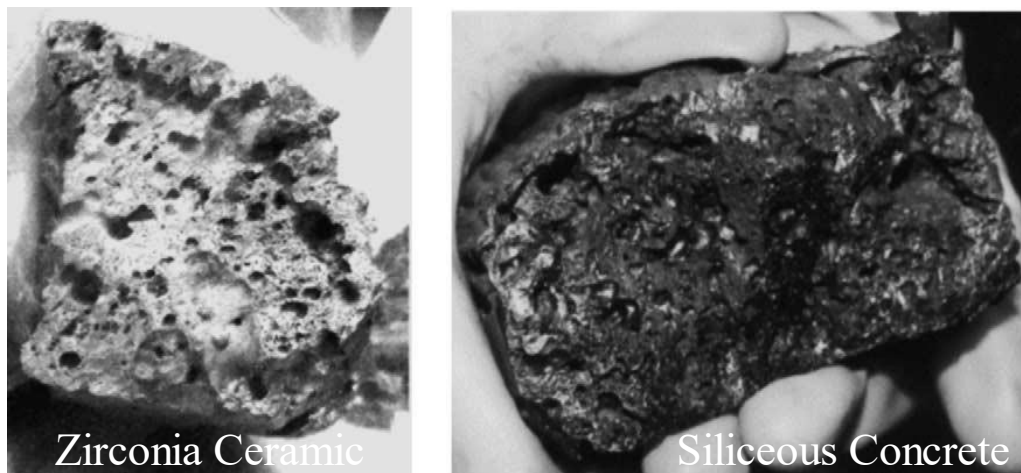
Figure 18 Pores found in VE-U7 postmortem result (Journeau, Haquet, Spindler, Spengler, & Foit, 2006)

3.2. Simulation condition of VULCANO VE-U7

In this study, two different types of analyses are carried out: the single-channel analysis and the double-channel analysis. The inflow and initial boundary conditions are summarized in **Table 1**. In the single channel analysis, only a single test section is modeled, and the inflow melt to the test section is

26

given as a boundary condition to investigate separate test effects due to different substrates as shown in *Figure 19a*. Based on VE-U7 data in (Journeau, Haquet, Spindler, Spengler, & Foit, 2006), the geometry test section has been designed to guarantee identical hydraulic flows on both channels, at least experiment result showed that at the first 8s the corium spreading on both channels have the same velocity. With consideration of constant flow rate during this period, a mean mass flow rate of 1.75 kg/s is used for corium spreading over both the ceramic and concrete channels in this study. The inflow melt temperature is determined as 2,450 K, which is the best estimate from the measurement. It is noted that the total pour mass given in Table 1 is defined as the total mass in the two test sections for the single channel analyses, which excludes the residual mass in the stabilization pool (Journeau, Haquet, Spindler, Spengler, & Foit, 2006). On the other hand, the definition of the total pour mass is the mass which has been poured into the stabilization pool, after which the overflowing melt is directed to the two test sections.

For the double channel analysis, the two channels and the stabilization pool are modeled to consider inflow mass interactions of the two channels, as shown in *Figure 19b*. In the real experimental set-up, the stabilization pool is 5.00 mm deeper than the spreading channel plans (Journeau, Haquet, Spindler, Spengler, & Foit, 2006). In present MPS simulation, the stabilization pool, ceramic, and concrete bottoms are assumed at the same height, and the total injected melt is 31.3 kg to neglect the small depth difference at bottom and save computation cost. With this modification, the mass into both channels could be kept around 26.6 kg, which is consistent with the total mass spreading on concrete and ceramic channels in single-channel analysis. The remaining mass 4.7 kg is in the stabilization pool. In single-channel analysis, the stabilization pool is not necessary and not modeled. In the double channel analysis, the stabilization pool is indispensable because it enables the mass flow interaction between two channels. The pouring rate is determined by assuming uniform injection to the stabilization pool in 7.3 s, which gives an inflow mass flux of 4.3 kg/s. To assure the same inflow melt temperature to the test sections as defined in the single channel analysis, the stabilization pool is assumed to be adiabatic at 2,450 K.
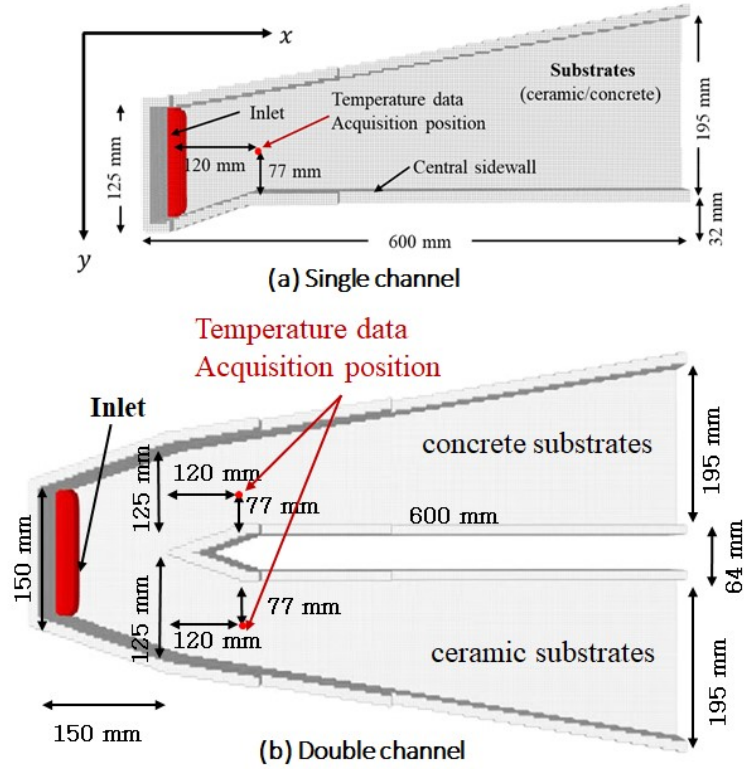
Figure 19 Calculation geometry of MPS simulations for VULCANO VE-U7 experiment.

Table 1 Inflow and initial boundary conditions

	Single channel analysis	Double channel analysis
Total pour mass (kg)	14.0 (to the ceramic channel) 12.6 (to the concrete channel)	31.3 (to the stabilization pool)
Inlet mass flux (kg/s)	1.75 (to the test section)	4.30 (to the stabilization pool)
Inlet melt temperature (K)	2,450	2,450
Initial substrate temperature (K)	300	300

3.3. Thermo-physical properties

The average composition of the prototypic corium of VULCANO VE-U7 was, in mass percentage, 56% UO_2, 32% ZrO_2, 5% FeO, 2% $CaSiO_3$, 2% SiO_2, 1% Fe, 1% CaO, and 1% Al_2O_3, which represented a mixture of corium with the EPR reactor pit sacrificial material which is designed to condition corium for the core catcher (Journeau, Haquet, Spindler, Spengler, & Foit, 2006). According to the literature (Journeau, Haquet, Spindler, Spengler, & Foit, 2006), the initial, liquidus and solidus temperatures of the melt were 2,450 K, 2,623 K and 1,273 K, respectively and solid fraction of the melt has been evaluated as a function of its temperature (indicating that the inflowing melt was already 50 % solidified) (see *Figure 20*). In this study, the following polynomial approximation has been adopted to fit with the previous evaluations.

28
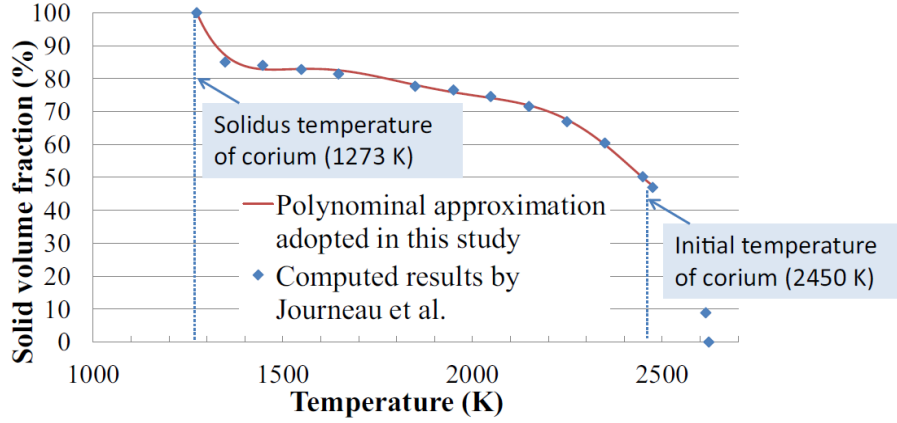
Figure 20 Solid volume fraction of corium with respect to temperature

$$\gamma = 425.065024 - 1.375802897T + 1.84196 \times 10^{-3}T^2$$
$$- 1.30294 \times 10^{-6}T^3 + 5.13559 \times 10^{-10}T^4 \qquad (39)$$
$$- 1.06944 \times 10^{-13}T^5 + 9.19116 \times 10^{-18}T^6$$

Based on this evaluation, the viscosity of the melt is evaluated as a function of solid fraction. The Ramacciotti's model (Ramacciotti, Journeau, Sudreau, & Cognet, 2001) is widely adopted for evaluating the viscosity increase in the solidification interval. In this study the following model is used, which considers correction to the original Ramacciotti's model with a bubble factor (B_μ) to represent the viscosity-increase as also used in LAVA simulation of VE-U7 [Journeau, Haquet, Spindler, Spengler, Foit, 2006]:

$$\mu(T) = B_\mu \cdot \mu_{liq} \exp\left(2.5. C. \gamma(T)\right) \qquad (40)$$

Where μ_{liq} is the kinematic viscosity of the liquid phase; C is a parameter depending on the types of corium, and $\gamma(T)$ is solid fraction. The melt will be no longer spreadable when γ(T) is larger than a critical value of immobilization solid fraction (γ_c), where the calculated viscosity will be increased by 100 times to stop the spreading. In this paper, the best estimated value of parameter $C = 6$ and $\gamma_c = 80\%$ are adopted based on the MPS sensitivity analysis done by Duan, at. al (Duan, Yamaji, & Koshizuka, A Novel Approach for Crust Behaviors in Corium Spreading Based on Multiphase MPS Method, 2018b) and also as estimated by LAVA (Journeau, Haquet, Spindler, Spengler, & Foit, 2006). In this study, the value of the bubble factor (B_μ) is determined through sensitivity analysis which will be explained in section 4.4. The bubble factor is merely a simple multiplication factor representing a viscosity increase due to the bubble effect, which is also used in the reference in (Farmer, Melt Spreading Code Assessment, Modifications, and Applications to the EPR Core Catcher Design, 2009;

29

Spindler & Veteau, Simulation of spreading wiht solidification: assessment synthesis of THEMA code, 2004; Ye, et al., 2013; Journeau, Haquet, Spindler, Spengler, & Foit, 2006).

The other thermo-physical properties of corium and substrates used for this study are summarized in **Table 2**. These data are used as constant parameters. In this study, melting (ablation) of the concrete substrate is not considered, because the post-test ablation was not significant (a few millimeters) as discussed in (Journeau, et al., 2003).

Table 2 *Thermo-physical properties (Journeau, Haquet, Spindler, Spengler, & Foit, 2006)*

	Corium	Ceramic substrate	Concrete substrate
Density [kg/m^3]	7140	5300	2475
Thermal conductivity [W/m/K]	3.0	4.7	1.3
Specific heat [J/kg/K]	800	575	750
Emissivity	0.8	Not considered	Not considered
Solidus temperature [K]	1273	Not considered*	Not considered*
Liquidus temperature [K]	2623	Not considered*	Not considered*
Fusion enthalpy [kJ/kg]	420	Not considered*	Not considered*
Viscosity of liquid (Pa.s)	0.0206	Not considered*	Not considered*

*) The melting of substrates is not considered in this study.

3.4. Result and discussion
3. 4.1. Calculation resolution

According to the posttest examination, the solidified melt thickness ranged from about 50 to 70 mm and the final spreading distance was 450 mm and 360 mm for the ceramic and concrete channels, respectively. The particle size has to be sufficiently small to resolve the melt in the thickness direction, and the evaluated spreading distance should sufficiently converge with the particle size to resolve the final spreading distance difference between the two channels.

The focus of this study is to explore melt crust interactions during corium spreading when the melt rheology is influenced by gas bubbles. Hence, representation of the free surface crust layer is necessary. As the particle size is reduced to around 5 mm, the crust formation at the free surface is clearly reproduced as will be discussed in Section 4.2. In terms of quantitative numerical convergence, *Figure 21* shows calculated spreading distance for the ceramic channel with time for different particle sizes. As shown, the final spreading distance tends to convergence with reducing particle size. For the cases with particle sizes of 3 mm and 2 mm, the difference in the evaluated final spreading distance is as small as about 15 mm. In contrast, the measured final spreading distance difference between the ceramic and concrete channels is about 91 mm, which is much larger than the expected numerical

uncertainty. Thus, with the above considerations and with the practical availability of computation power, this study adopts the reference particle size of 3 mm. The adopted reference particle size of 3 mm is consistent with those adopted by the preceding studies (Yasumura, Yamaji, Furuya, Ohishi, & Duan, 2017; Duan, Yamaji, & Koshizuka, A novel multiphase MPS algorithm for modeling crust formation by highly viscous fluid for simulating corium spreading, 2019), which were 3 mm to 5 mm.
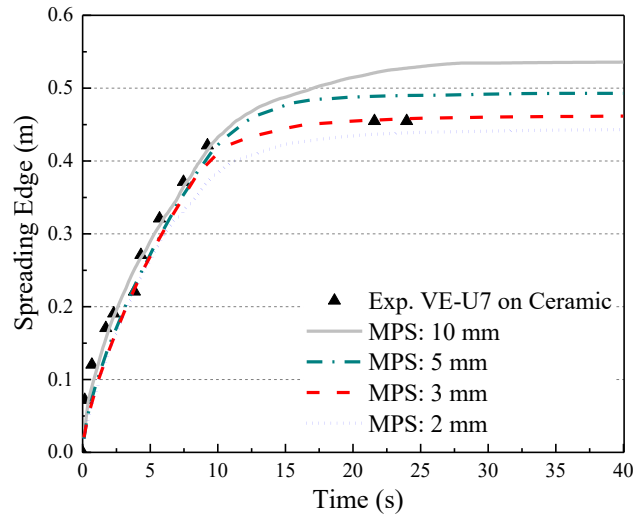
Figure 21 Spreading edge with different particle sizes for the ceramic channel

3. 4.2. Single channel analysis

In this chapter, single channel analysis results are presented to discuss separate effects of the followings on the melt spreading profiles and the substrate temperature development:

(1) Particle size (calculation resolution)

(2) Contact thermal resistance between the melt/curst and the substrate

(3) Total melt pour mass

(4) Possible gas bubble effects represented by:

   (a) Increased effective viscosity of the melt

   (b) Increased effective thermal conductivity of the melt

   (c) Increased effective emissivity of the melt

3.4.2.1. Influence of melt-substrate thermal resistance model

As discussed in the preceding study, ablations of the substrates were limited, even for the concrete substrate, and their influences may be negligible (Journeau, et al., 2003). In this situation, it may be appropriate to tune the contact thermal resistance between the melt/crust and the substrate without consideration for melting of the substrate so that the calculated substrate temperatures, at the locations shown in *Figure 19*, match those of the measurements. Thus, the best estimate thermal contact

resistances for the ceramic and concrete substrates have been determined as 2.0×10^{-3} Km^2/W and 1.0×10^{-3} Km^2/W, respectively as shown in *Figure 22*. However, it should also be noted that for the concrete substrate there may have been slight ablation which was not considered in the simulation and the heat contact resistance is probably not constant in reality. As can be seen from Fig. 22(b), the substrate temperature at 2 mm depth is better predicted with assumption of zero contact thermal resistance for the first 12.5s but overestimated after that. The overall trend is better reproduced by assumption of 1.0×10^{-3} Km^2/W. Thus, in this study, the constant thermal resistance of 1.0×10^{-3} Km^2/W is assumed for the concrete substrate as this study is mainly focused on the late termination phase of the spreading.

(a) Ceramic substrate   (b) Concrete substrate
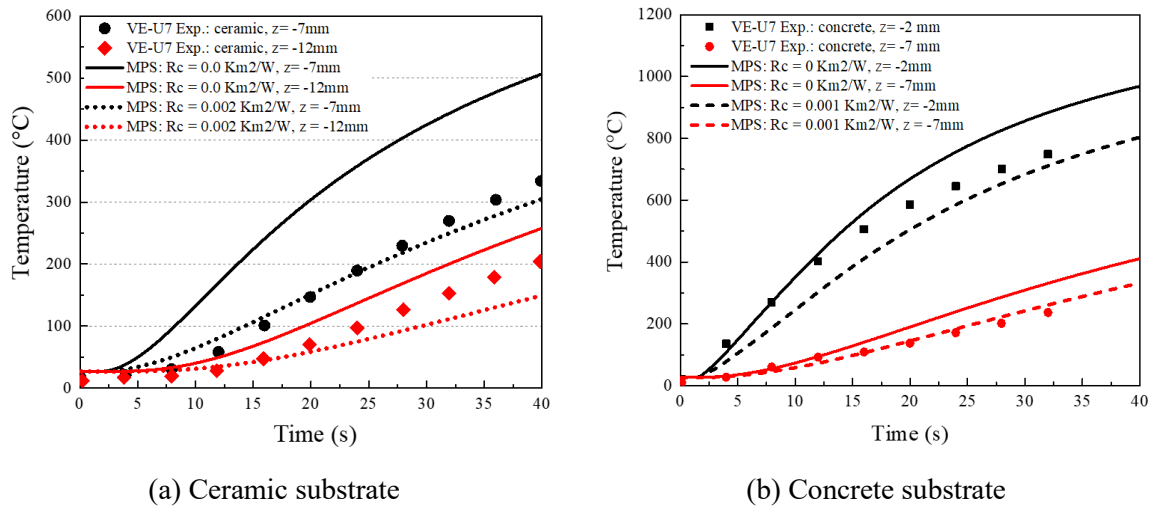
Figure 22 Substrate temperature changes with time

In the meantime, the influence of the contact thermal resistance on crust formation and spreading behavior is investigated. *Figure 23* shows cross-sectional views of MPS analysis results at the time of termination of the spreading (t=20s) for the two cases with different contact thermal resistances (0 and 2.0×10^{-3} Km^2/W) of the ceramic channel. The results show that the contact thermal resistance influences development of the thin crust layer at the melt-substrate boundary, but it does not have significant influence on the crust formation at the leading edge and the bulk melt temperature profile. As the result, the spreading behavior is hardly affected by the contact thermal resistance as also shown in *Figure 24*. Hence, the current MPS simulations indicate that difference in contact thermal resistance is not likely to be the main cause of the spreading difference between the ceramic and concrete channels.
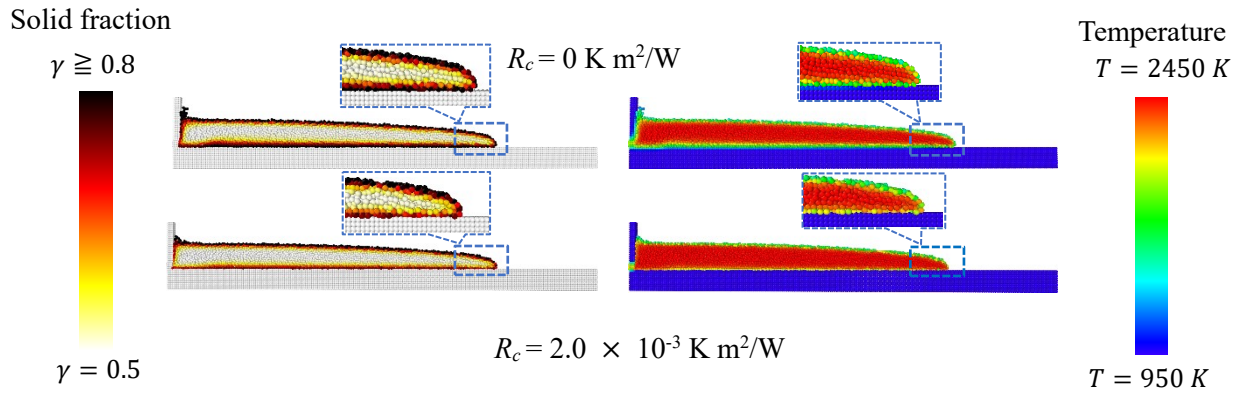
Figure 23 Cross sectional distribution of solid fraction and temperature at t=20s
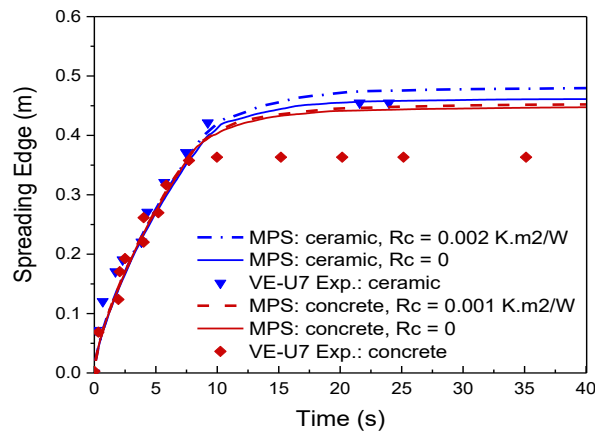
Figure 24 Influence of contact thermal resistance on spreading edge

It is noted that the simulated spreading profile over concrete obviously deviates from experimental measurements because the bubble effect which was clearly observed in the experiment is still not considered. The bubble effect will be considered in Section 4.4 for single-channel analysis and in Section 5 for double-channels analysis.

3.4.2.2. Influence of total melt pour mass

In the experiment, it was observed that the inflow mass and spreading behavior were basically the same until the late phase, when termination of the spreading of the concrete channel apparently induced some additional inflow mass to the ceramic channel via the stabilization pool, which may have contributed to the prolonged spreading of the ceramic channel. The final total melt pour masses to the ceramic and concrete channels were 14.0 kg and 12.6 kg, respectively. In some studies, the difference in the total melt pour mass of 1.4 kg is suggested as the main cause of the difference in the spreading between the two channels (Journeau, Haquet, Spindler, Spengler, & Foit, 2006). Such possibility is

33

investigated with the present MPS method.

Figure 25 shows spreading edge development with time for the ceramic and concrete channels with different total melt pour masses. The total melt pour masses were hypothetically increased or decreased by 1.4 kg to investigate its sensitivity on the spreading. The melt pour duration was changed while keeping the melt pour mass flux unchanged. The results indicate that uncertainty in the total melt pour mass is not sufficient to explain the final spreading distance difference.

(a) Ceramic substrate   (b) Concrete substrate
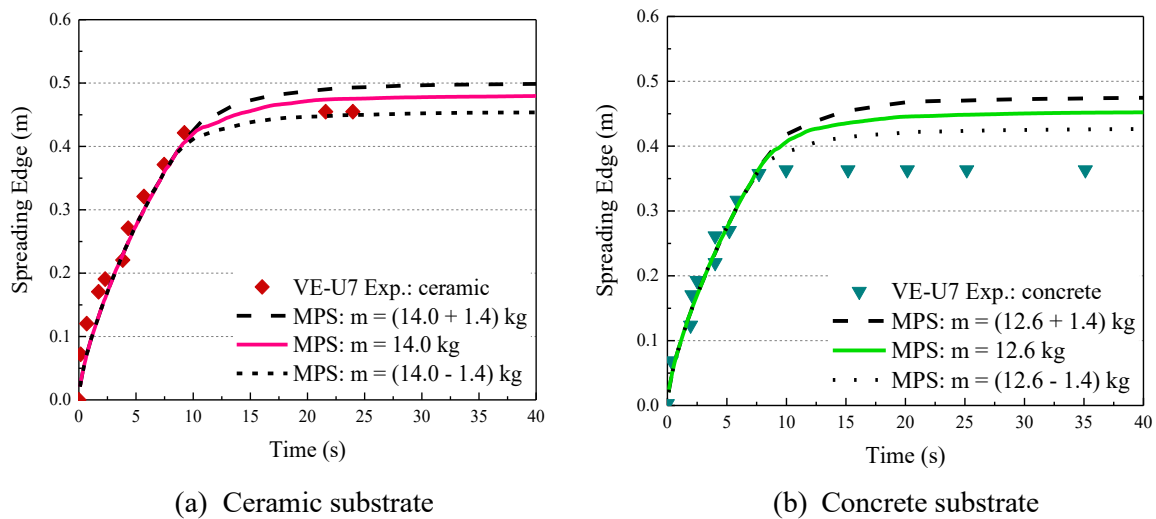
Figure 25 Influence of total melt pour mass on spreading profiles

3.4.2.3. *Influence of gas bubble on corium spreading over the concrete substrate*

As discussed in (Ramacciotti, Journeau, Sudreau, & Cognet, 2001; Manga & Loewenberg, 2001; Mader, Llewellin, & Mueller, 2013), the existence of bubbles can increase the viscosity of isothermal flow. The assumed reason behind the parametric study is that, basically, gas bubbles are considered to be able to squeeze the melt in the thickness direction and consequently, flow resistance of melt could be increased due to the narrowed cross section of melt flow. In the past studies, the bubble effect is considered by enhancing the effective viscosity in (Farmer, Melt Spreading Code Assessement, Modifications, and Applications to the EPR Core Catcher Design, 2009; Spindler & Veteau, Simulation of spreading wiht solidification: assessment synthesis of THEMA code, 2004; Ye, et al., 2013; Journeau, Haquet, Spindler, Spengler, & Foit, 2006). The rising of bubbles from the bottom to the free surface can agitate the spreading flow, causing a transition from the laminar flow to the gas-liquid two-phase turbulent flow, which can significantly enhance convective heat transfer inside the flow. Therefore, enhancing the overall effective conductivity is also a main effect of gas release. The enhancement of heat transfer between the melt and the substrate is utilized in THEMA simulation (Spindler & Veteau, Simulation of spreading wiht solidification: assessment synthesis of THEMA code, 2004) but without detailed analysis. In addition, the bubble burst at the free-surface can increase the surface area, which

can enhance the radiation heat loss and be modeled by the increase of effective emissivity. Hence, in this study, the separate effect of the gas bubble is studied by increasing the following parameters of the melt independently: the effective viscosity, the thermal conductivity, and the radiation emissivity.

The reference case corresponds to the case, in which the melt conductivity is 3.0 W/m/K, radiation emissivity is 0.8, and the bubble factor B_μ in Eq. (40) is 1.0. *Figure 26* shows snapshots of the cross-section view of spreading at representative moments for the reference case and the three separate effect test cases. The sensitivity cases correspond to the circumtance, in which the effective viscosity, the effective conductivity, and the effective emissivity are multiplied by factors of 3, 80 , and 5, respectively. These multiplications factors are hypothetically determined so that the calculated final spreading distance agrees with the measurement. It is only intended to show the qualitative influence of these factors on corium spreading.

In reality, the gas bubble effects may result in combinations of these factors. Furthermore, the gas bubble effects should be localized to the melt near the gas bubbles. It should be noted that mechanical modeling of the gas bubble and the melt interactions is beyond the scope of the current study. Instead, this study takes the classical approach as adopted by many other researchers to model global influence of the gas bubbles on the melt rheology, such as by multiplying the effective viscosity, emissivity and thermal conductivity of the melt. In addition, the emissivity would unphysically be above 1.0 as a simplified way to express the increased radiation due to the increased surface area in case of bubbling.

$\gamma = 0.5$ ... $\gamma \geqq 0.8$

Representative moment of the gravity-inertia phase — t=1.0 s

Representative moment of the gravity-viscous phase — t=8.0 s

Representative moment of termination phase — t=15.0 s

(a) Reference case ($B_\mu = 1.0; k = 3.0$ W/m/K; ε=0.8)

(b) Viscosity is multiplied by 3 ($B_\mu = 3.0$)

(c) Conductivity is multiplied by 80 ($k = 240.0$ W/m/K)

(d) Emissivity is multiplied by 5 (ε=4.0)
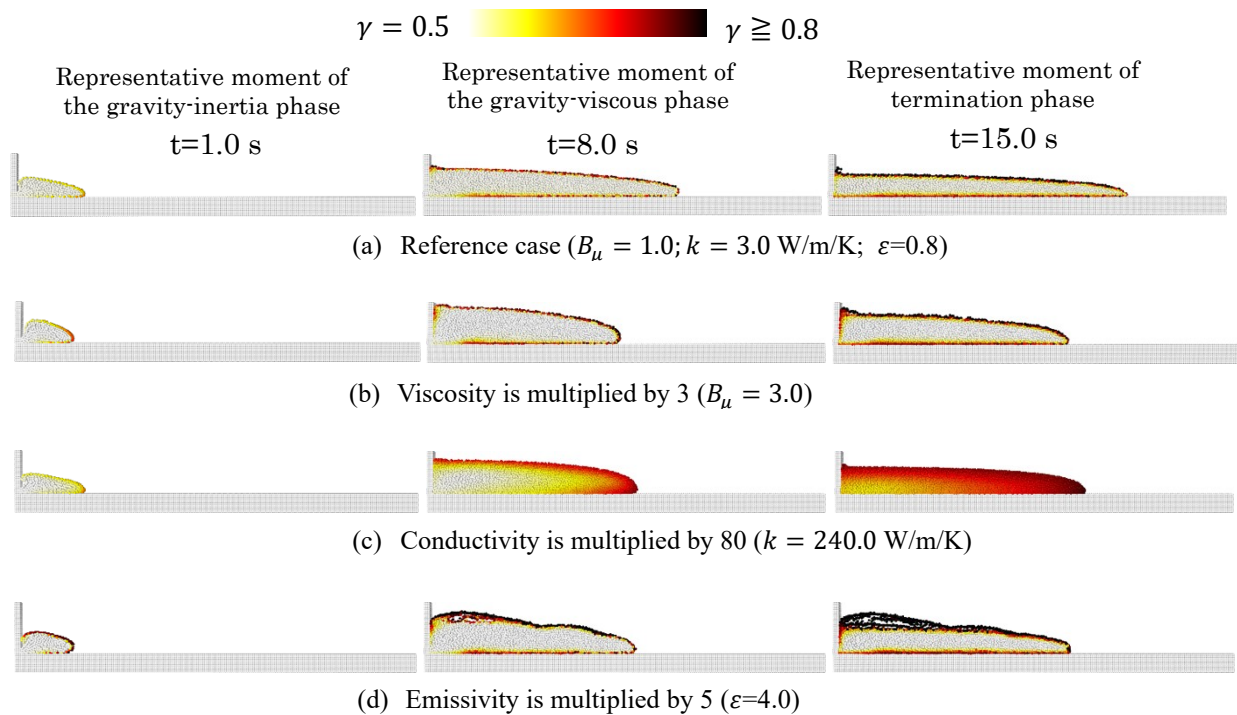
Figure 26 Snapshots of cross-section view of spreading at representative moments

When the effective viscosity is increased, the spreading is hindered by the increased viscosity of the bulk melt. In the meantime, increasing the effective conductivity has the effect of increasing the bulk melt viscosity by reducing the temperature gradient from the melt surface (crust) to the bulk melt. At the same time, crust formation at the melt surface is delayed. In contrast, increasing the effective emissivity has little influence on the bulk melt, but promotes crust formation at the melt surface.

For quantitative comparisons, sensitivities of increasing the effective viscosity, conductivity and emissivity on the spreading edge profiles are shown in *Figure 27*. All results show that spreading is hindered towards the late phase of the spreading and adjustments with any of the three parameters can produce similar results. However, it is difficult to identify which of the three is the dominant effect of gas release.
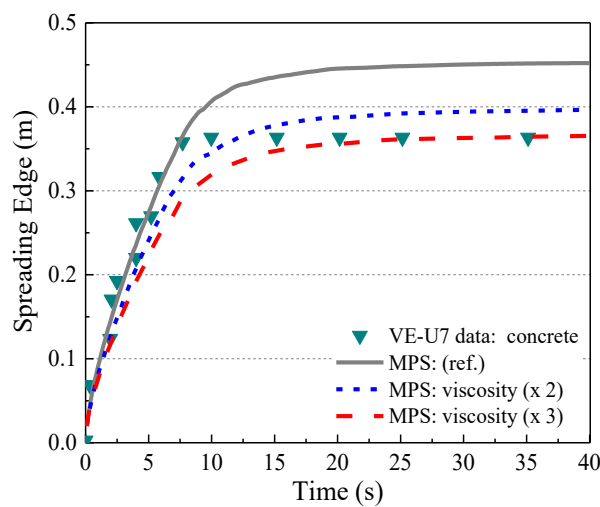
(a) Viscosity is multiplied by 3 (B_μ=3.0)
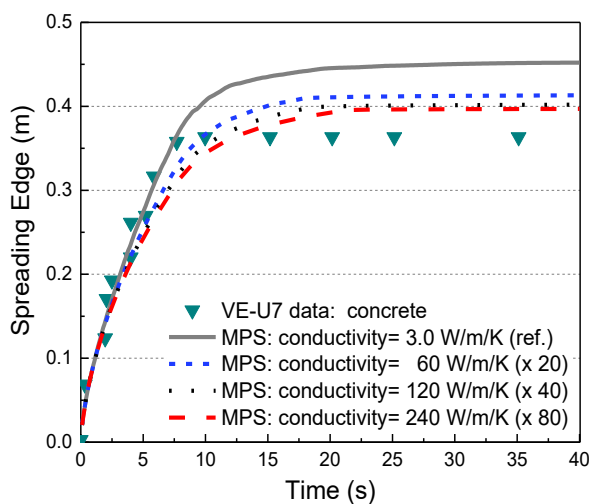
(b) Conductivity is multiplied by 80 (k=240 W/m/K)
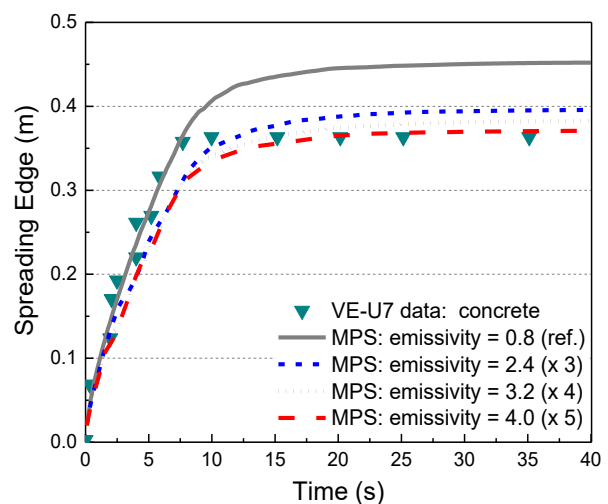
(c) Emissivity is multiplied by 5 (ε=4.0)

Figure 27 Influence of bubble gas presence on spreading edge over concrete substrate (single channel analysis)

3. 4.3. Double channels analysis

3.4.3.1. *Gas bubble effects with coupling of the two channels*

As discussed in Chapter 4, the single channel analyses with MPS method shows that the potential spreading difference between the two channels of VULCANO VE-U7 is not likely to be due to the difference in the contact thermal resistance and not likely to be solely due to the total inflow mass difference. The results show that the gas bubble effects on the concrete channel may have affected the spreading to some extent. However, as discussed in Section 4.3, the spreading in the two channels was actually not independent in the experiment, but coupled through the melt inflow from the stabilization pool. Hence, this section discusses whether the three gas bubble effects may have different impacts on the spreading through a coupling of the two channels with double-channel analyses with the geometry as shown in *Figure 19b*.

The top views of the four different simulation cases at the time of spreading termination are shown in *Figure 28*. The four cases are: (a) the reference case; (b) viscosity is multiplied by 3 (B_μ =3.0); (c) conductivity is multiplied by 80 (k=240 W/m/K); (d) emissivity is multiplied by 5 (ε=4.0). When the gas bubble effects are not considered (reference case), the different contact resistance and thermo-physical properties (conductivity and specific heat) of the different substrates hardly shows any difference on the spreading profiles (*Figure 28a*). Then, as also indicated by the single channel analyses, the sensitivity cases with different gas bubble effect parameters show shorter spreading distances for the concrete channel, compared with those of the ceramic channel. However, the set of parameters, which resulted in almost the same final spreading distances with the single channel analyses, resulted in quite different final spreading distances.

More understanding of the differences among the three sensitivity cases can be gained from the spreading edge profiles as shown in *Figure 29*. These figures show that when the effecitve viscosity or emissivity of the melt is increased for the concrete channel, spreading is hindered from the early phase. These differences in the early phase of the spreading can also be found in the single channel analysis results (*Figure 27a* and *Figure 27c*), but the differences are not as evident as those in the double channel analyses results. These results indicate that slight spreading difference in the early phase can develop with time to large difference through the inflow melt mass flux interaction at the stabilization pool. In contrast, the experimental measrements show that the spreading in the two channels were almost the same until the late phase. Such delayed influence on spreading can be well reproduced when the effective conductivity of the melt is increased as shown in *Figure 29b*. These results are also supported by the evaluated final melt masses spreading on the ceramic and concrete channels, where final mass of 14.01 kg and 12.58 kg, respectively, is shown by the late case only (see *Figure 29b*).

$\gamma = 0.5$ $\gamma \geqq 0.8$

(a) Ref. case ($B_\mu = 1.0; k = 3.0$ W/m/K; $\varepsilon=0.8$)   (b) Viscosity is multiplied by 3 ($B_\mu = 3.0$)

(c) Conductivity is multiplied by 80 ($k = 240$ W/m/K)   (d) Emissivity is multiplied by 5 ($\varepsilon=4.0$)
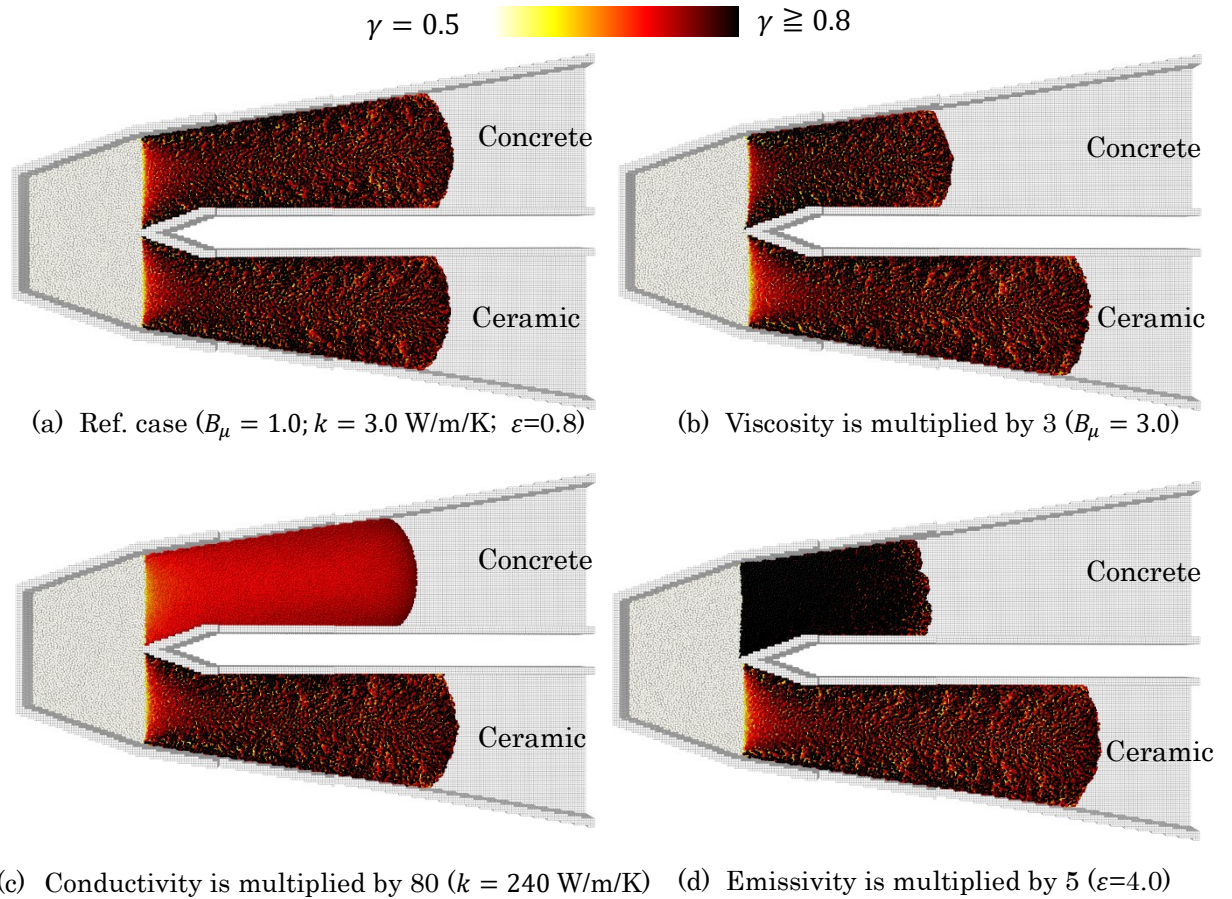
Figure 28 Top view at the time of spreading termination (t=15s)

(a) Viscosity is multiplied by 3 (B_μ=3.0)

(b) Conductivity is multiplied by 80 (k=240 W/m/K)   (c) Emissivity is multiplied by 5 (ε=4.0)

Figure 29 Influence of bubble gas presence on spreading edge over concrete substrate (double channel analysis)

3.5. Discussion on possible mechanism

Through the single-channel and double-channel analyses, it has been indicated that the potential spreading difference between the two channels of VULCANO VE-U7 is not likely to be due to the difference in the contact thermal resistance and not likely to be solely due to the total inflow mass difference. It has been indicated that the difference is due to some gas bubble effect on the concrete channel, which induced some delayed resistance to the flow that only became significant towards the termination phase of the spreading. Such delayed resistance could not be reproduced by increasing the melt effective viscosity or emissivity by constant factors, but could be well reproduced by increasing the effective conductivity of the melt. For clarifications, the terms used in this context as "effective viscosity", "effective conductivity," and "effective emissivity" may be understood as following possible physical phenomena:

- Effective viscosity: the existence of bubble can increase the viscosity of isothermal flow. Gas bubbles can squeeze the melt in the thickness direction, and consequently, the flow resistance of melt could be increased due to the narrowed cross section of melt flow (Ramacciotti et al., 2001; Manga and Loewenberg, 2001; Mader et al., 2013).

- Effective conductivity: The rising of bubbles from bottom to the free surface can agitate the spreading flow, causing a transition from the laminar flow to the gas-liquid two-phase turbulent flow, which can significantly enhance convective heat transfer inside the flow (Farmer, 2009; Spindler and Veteau, 2004; Ye et al., 2013; Journeau et al., 2006).

- Effective emissivity: The bubble burst at the free surface can increase the surface area, which can enhance the radiation heat loss and be modeled by the increase of effective emissivity.

In the MPS method, convection of the resolved scale is considered by the particle movement. In this study, the subscale convection is modeled by increasing the effective thermal conductivity of the particle (melt). This is intended to model the influence of the rising of gas bubbles from the concrete substrate to the melt free surface, which agitates the spreading flow, causing a transition from the laminar flow to the gas-liquid two-phase turbulent flow, which can significantly enhance convective heat transfer inside the flow. As a result, the bulk melt solid fraction is increased (viscosity is increased) while the crust formation at the melt surface is delayed (*Figure 28c*). The combined effect of these was not significant until the late phase of the spreading, when the crust at the leading edge has sufficiently developed to terminate the flow.

However, it should be noted that there is large uncertainty with the viscosity of the melt. In this study, the viscosity of the prototypic corium used in VULCANO VE-U7 is modeled with the modified Ramacciotti's correlation, in which the gas bubble effect on viscosity is considered with a constant factor (B_μ). It may well be that the viscosity of the specific melt behaves in such a way that the gas bubble increases the viscosity more sharply towards the late phase of the spreading. Another possibility is that there may have been some delay until significant gas bubbles were generated from the concrete substrate after the melt has spread, as there needs to be some time before the concrete heat up to the decomposition temperature.

In any case, for VULCANO VE-U7, this study has shown that a slight spreading difference in the early phase can develop with time to a large difference between the two channels. Hence, analyses that can consider inflow mass interactions at the stabilization pool are necessary to investigate the difference between the two channels.

In the current study, the effect of the gas bubbles are idealized by separate treatment with respect to enhanced effective viscosity, emissivity, and conductivity as also considered in the preceding studies (Farmer, Melt Spreading Code Assessement, Modifications, and Applications to the EPR Core Catcher Design, 2009; Spindler & Veteau, Simulation of spreading wiht solidification: assessment synthesis of THEMA code, 2004; Ye, et al., 2013; Journeau, Haquet, Spindler, Spengler, & Foit, 2006)". It should be noted that, in reality, all these three parameters may not be independently changed by the gas bubbles. The principal mechanism of increased viscosity with gas bubbles may be narrowing down of the melt in the thickness direction, which may result in increased flow resistance. In the meantime, the rising of bubbles may also agitate the spreading flow, causing a transition from the laminar flow to the gas-liquid two-phase turbulent flow, which may significantly enhance convective heat transfer inside the flow. In general, as pointed out by Kays (Kays, 1994), it is difficult to correlate the order of magnitudes of these effects or assume independence of these effects.

However, investigations on the microscale phenomenological effect of gas bubbles on the melt are beyond the scope of the current simulation with limited resolution. Thus, the classical approach as also taken by the preceding studies is employed. The focus of this study is on enhancing capability of

MPS method for exploring corium spreading difference between different substrates. With the newly developed thermal contact resistance model, the capability of MPS has been improved to consider different interface heat transfer effects. This enabled discussions on melt / substrate heat transfer, free surface crust formation, and the bulk melt property (viscosity) changes on the corium spreading together with mechanical modeling of melt / crust interactions. Furthermore, the importance of considering the inflow melt interactions at the stabilization pool is highlighted for the VULCANO VE-U7 configuration.

3.6. Conclusion

The potential differences between melt spreading over the inert ceramic channel and concrete channel have been investigated with the improved MPS method, which can now consider thermal contact resistance between the melt / crust and the substrates. The following conclusions can be drawn for VULCANO VE-U7 spreading, which can be featured with almost identical spreading leading edge propagation of the two channels until the late phase of the spreading, when the spreading of the concrete channel is suddenly hindered relative to that of the concrete channel.

The different mechanisms could not be well identified with the single channel analyses. The double channel analyses were necessary to narrow down the different possibilities, because it was necessary to consider the inflow mass interactions at the stabilization pool. The analysis results indicated that the difference is not likely to be due to the difference in the contact thermal resistance and not likely to be solely due to the total inflow mass difference. The delayed hindering of spreading in the concrete channel in the late phase of the spreading could be well explained by the enhanced effective thermal conductivity of the melt (which may be explained in terms of gas bubble agitated internal convection of the melt). The enhancement has the effect of increasing the bulk melt viscosity while the crust development at the melt surface is delayed. As a result, the simulated spreading of the two channels was almost identical until the late phase, when early termination in the concrete channel induced inflow mass to the ceramic channel from the stabilization and prolonged the ceramic channel spreading.

While the above mechanism has been indicated in this study, the current MPS simulation does not consider other possibilities/factors, which may be worth for further investigations. For example, there may be some time delay before the concrete substrate heat-up and significant gas bubbles are generated after the melt spreading. There is also large uncertainty with the estimated melt viscosity. These uncertainties may also be responsible for the delayed spreading hindering in the concrete channel.

Chapter 4 Simulations of ECOKATS-V1 test with MPS Method

4.1. Test description of ECOKATS-V1

The characteristics of the ECOKATS-V1 test (Alsmeyer, et al., 2004) are melt spreading with a low flow rate (1.36 liter/s), using superheated melt (70 K higher than liquidus temperature) with an initial temperature of 1,893 K, narrow liquid-solid phase change (450 K), and several crust fractures being observed. The test section was 8 m in length over 0.250 m in width of parallel channel with ceramic floor and concrete sidewalls. The high-temperature melt was released from the thermit crucible vessel to the whirl basin, then spread to the spreading channel (see *Figure 30*). The mass of the thermite vessel was measured during the outflow time of the melt. The initial temperature was recorded from the W-Re thermocouple installed in the whirl basin. The composition of simulant oxide melt in ECOKATS-V1 in mass percentage was 41% Al_2O_3, 24% FeO, 19% CaO, and 16% SiO_2. According to the literature (Alsmeyer, et al., 2004), the liquidus and solidus temperatures were 1,822 K and 1,373 K, respectively. The main purpose of ECOKATS-V1 experiment was as a pre-test to investigate the rheological behavior of the simulant oxide melt. This simulant melt then was intended to be used for large scale spreading experiments in ECOSTAR project.
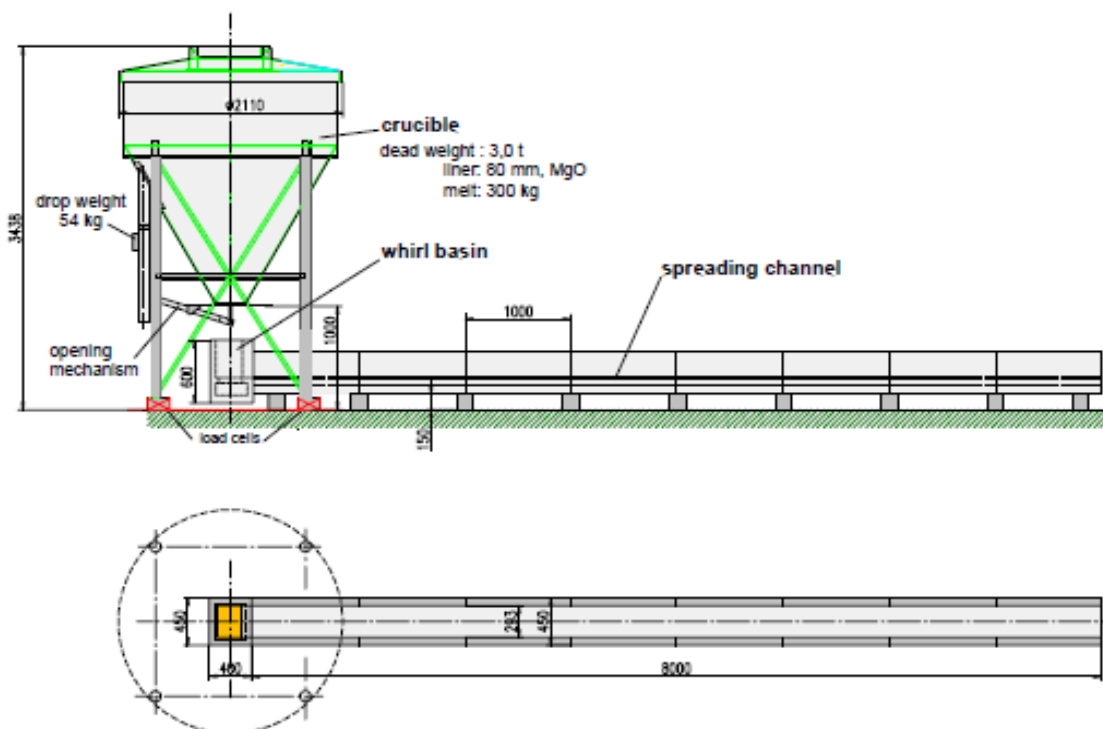
Figure 30 ECOKATS-V1 experimental setting and result (Alsmeyer, et al., 2004)

4.2. Simulation condition of ECOKATS-V1

In this study, the ECOKATS-V1 experimental setup is modeled with 2D simulation geometry, as shown in *Figure 31* with the initial conditions described in *Table 3*. The simulations were conducted for the first 100 s of the total spreading period.
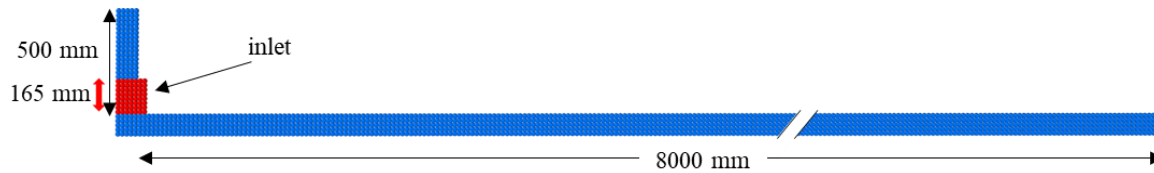
Figure 31 Two-dimension calculation geometry for ECOKATS-V1 test

Table 3 Initial boundary condition (Alsmeyer, et al., 2004)

Total inflow melt mass (kg)	193
Inlet mass flux (l/s)	1.36
Inlet melt temperature (K)	1,893
Initial substrate temperature (K)	300

The viscosity of the melt is evaluated as a function of the solid fraction by adopting Ramacciotti's model (Ramacciotti, Journeau, Sudreau, & Cognet, 2001) as shown in Eq. (41):

$$\mu(T) = \mu_{liq} \exp\big(2.5.C.\gamma(T)\big) \tag{41}$$

where μ_{liq} is the kinematic viscosity of the liquid phase; C is an empirical parameter (tentatively, 3.0 in this study); The above-evaluated viscosity is increased by a factor of 10 when $\gamma(T)$ is larger than a predetermined critical value to represent crust. The corresponding viscosity is defined as the Solidification Viscosity Threshold (SVT) from hereinafter in the current study. The other thermo-physical properties of melt and substrates used for this study are summarized in *Table 4*. These data are used as constant parameters.

Table 4 Thermo-physical properties (Alsmeyer, et al., 2004)

	Melt	Ceramic Substrate
Density (kg/m³)	3,264	2,200
Heat conductivity (W/m/K)	5.4	3.8
Heat capacity (J/kg/K)	1,220	840
Emissivity	0.95	0.3
Liquidus temperature (K)	1,822	Not considered*
Solidus temperature (K)	1,373	Not considered*
Latent heat of fusion (kJ/kg)	1,162	Not considered*
Dynamic viscosity of melt (Pa.s)	0.2	Not considered*

*) The melting of substrates is not considered in this study.

4.3. Analysis result and discussion

The following analysis results are presented to discuss the influence of the crust formation and fracture on the ECOKATS-V1 spreading: (1) The influence of Particle size (calculation resolution); (2) The numerical stability improvement; and (3) Investigation on the influence of solidification viscosity threshold and the crust fracture stress.

4.3.1. Calculation resolution

The calculation resolution is investigated for different values of particle size from 1.7 mm to 4.0 mm without crust fracture model. The lowest spreading height in the simulation result is about 20 mm. It means if the resolution of 1.7 mm, 2.0 mm, 2.6 mm, or 4.0 mm particle size applied, there would be 11, 10, 7, or 5 particles along with the lowest height respectively. The result shows that the spreading profile seems converged to some extent when the particle size is smaller than "2 mm" (see *Figure 32*, although there are still remains some uncertainty in the final termination length (as will be discussed in the following sections, accurate prediction of the final spreading length is still beyond the capability of the current method in 2D modeling). Based on this result, the calculation resolution used after this section is using a particle size of 2 mm.
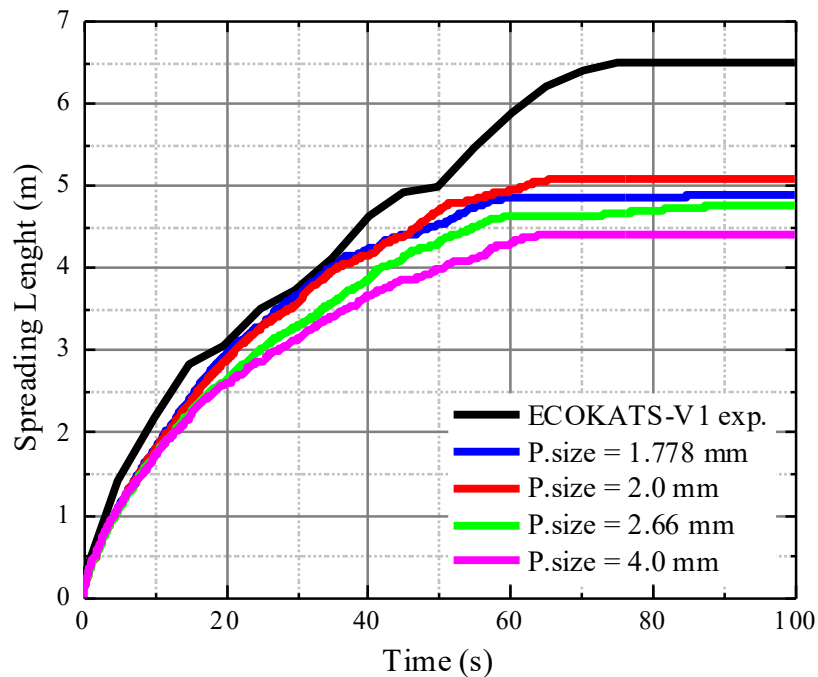
Figure 32 Sensitivity of calculation resolution

4.3.2. Numerical stability improvement with the new timestep control

The investigation of the impact for the new timestep control was conducted by comparing two cases, Case A and Case B, with the same maximum timestep at 0.001 s. Case A is simulated using traditional timestep control, where the timestep is controlled only by the Courant number condition. For Case A, instability happened at various moments due to locally fluctuated particle number density. As an example, the particle number density distribution at the time of 34.6 s is shown in *Figure 33*a. To avoid such instability, the maximum timestep had to be small enough (1.0e-4 s, in this case) to obtain numerically stable results, which required calculation time of 65 hours.

Meanwhile, Case B is simulated with the new timestep control, where the timesteps are controlled by a combination of Courant number control and PND control. When the calculated maximum PND is below the threshold (in this case, the $n_{threshold}$ is 20.2), the timestep is only controlled by the Courant number condition. When the maximum PND is above the threshold, then the PND control is activated with the minimum timestep limit of 1.25e-4 s. The result showed a stable simulation with a total calculation time of 37 hours (see *Figure 33b* and *Figure 34*). Thus, by applying the new timestep control technique, the numerical stability can be improved, and the calculation cost can be saved.

Case A → Traditional timestep control (Courant condition)

Particle Number Density

7.4   23.4

PND high regions that will result in numerical instability

(a) Case A

Case B → New timestep control (Courant condition + PND condition)
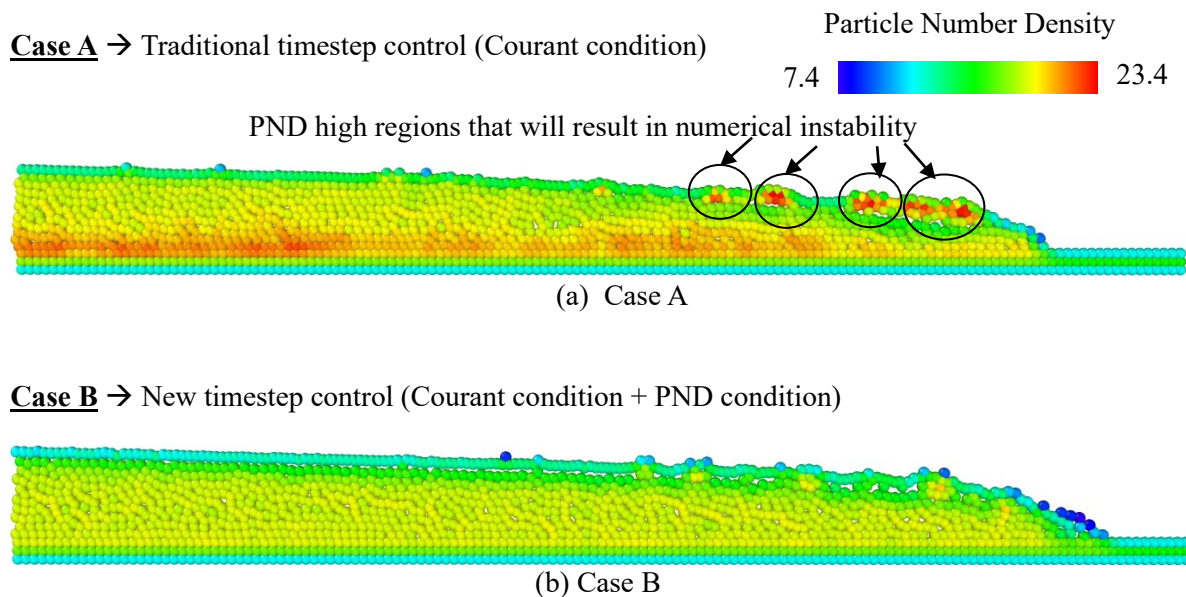
(b) Case B

Figure 33 Snapshot of particle number density distribution at 34.6 s
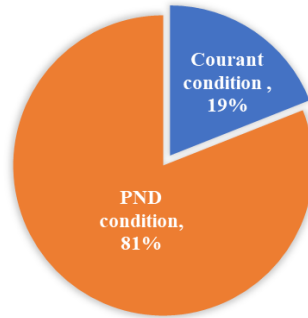
Figure 34   The appearance of each time-step control technique in Case B

Figure 35 shows that the spreading profile of case B is quite similar to the ones with case A, and the calculation results apparently show good agreement with the experiment results. However, the fact that the spreading profile agrees with the measured data does not necessarily mean that the simulation has captured the physical phenomena appropriately. The MPS with traditional time step control suffers from numerical instability and shows unphysical explosions from time to time. Such instability seriously limits the applicability of the method to further deepen understanding of corium spreading, which involves crust fracture (which is a physical phenomenon).
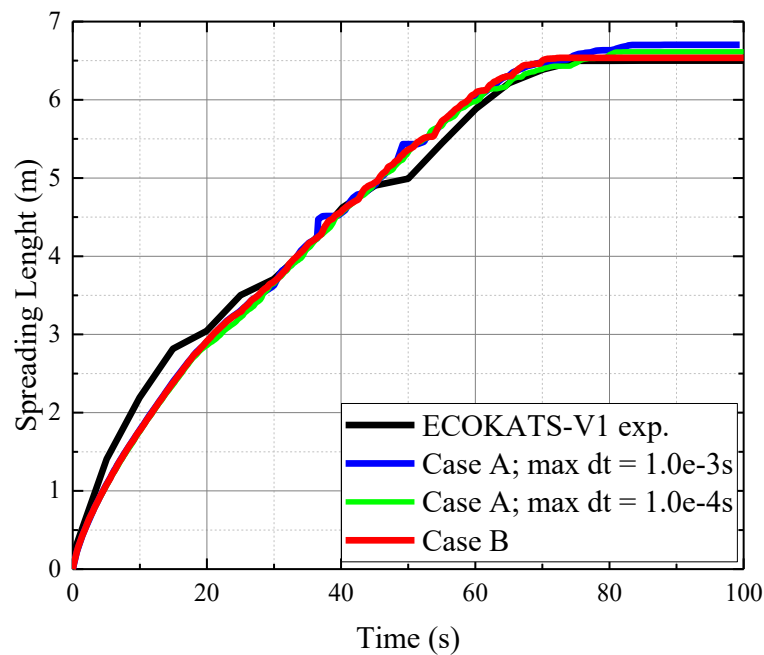
Figure 35 Spreading profile of case A (Courant condition) and case B (Courant + PND conditions)

4.3.3. Influence of solidification viscosity threshold and crust fracture stress

In the current MPS modeling, there are two important parameters in determining the spreading length and the crust behavior, namely the Solidification Viscosity Threshold (SVT) and the Crust Fracture Stress Threshold (CFST) of the melt. In principle, the higher the SVT is and the lower the CFST is, there is a tendency for the melt to be continuously spreadable without significant influence by crust formation and fracture. On the contrary, the lower the SVT is, and the higher the melt spreading behavior tends to be more determined by the crust formation and fracture.

The influence of different CFSTs (2,000 Pa; 4,000 Pa; 8,000Pa; 14,000 Pa) on the fracture patterns are investigated for the reference case (SVT: 1.8 Pa · s), as shown in *Figure 36*. The corresponding snapshots of the viscosity distributions indicate the fractured particles in red (i.e., fully melted particles). The results show that for the case with higher crust fracture stresses, the fractures tended to take place near the interface between the melt and the substrate at the leading front. In contrast, for the lower fracture stresses, the fractures tended to take place near the upper crust. The higher crust fracture stress cases seem to agree well with the movie taken during the experiment, which showed breaches near the melt-substrate interface. However, in the experiment, the fracture seemed to develop from the initial "weak spot." Such fracture development cannot be captured in the current 2-D simulation.
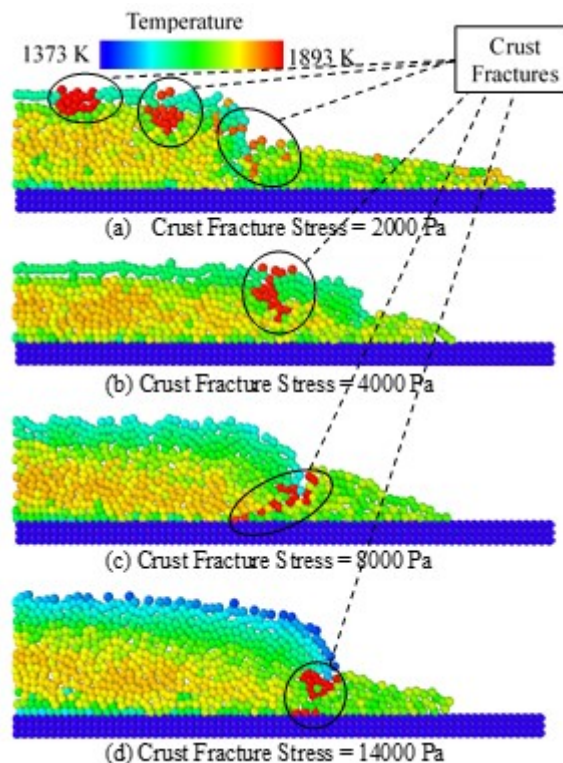
Figure 36 Snapshots of crust fracturing

In order to quantify the effects of SVT and CFST on the spreading behavior, a number of sensitivity analysis cases with different SVTs and the CFSTs are investigated. The spreading lengths of the sensitivity analysis cases are summarized in *Table 5*. As indicated in *Table 5*, the frequency of the crust fracture occurrence decreases with the increase of the CFST, and the readiness of the crust formation increases with the increase of the SVT. There are four highlighted cases that best reproduced the final spreading length measured in the ECOKATS-V1 experiment (6.50 m). The cases (CFST = 4,000 Pa, SVT = 1.8 or 7.9 Pa・s) reproduced the final spreading length measured in the ECOKATS-V1 experiment (6.50 m) with a number of crust fractures observed. On the other hand, for the other two cases, namely when SVT = 35.4 Pa・s　for CFST = 8,000 Pa and CFST = 14.000 Pa, crust fractures were not observed. This indicated that for a "stop and go" phenomenon during the melt spreading to be observed in the current MPS simulations a reasonable CFST value should be chosen. It should be noted that the combinations of the SVTs and CFSTs in these four best estimation cases do not reflect the real physical properties of the corium. Relationships between these numerical parameters and the rheology of the corium (especially with regard to crust formation and breach) need to be further investigated in future studies with 3D analysis modeling, as will also be discussed in the following sections.

Table 5 Spreading length (m) for some possible threshold combinations

Solidification Viscosity Threshold (Pa*s)	Crust Fracture Stress Threshold (Pa)									
	1,000		4,000		8,000		14,000		*Hardly formed*
1.8	6.92	m	**6.44**	**m**	5.83	m			↑
7.9	7.00	m	**6.54**	**m**	5.36	m	5.11	m	*Crust formation*
35.4			6.62	m	**6.50**	**m**	6.43	m	↓

More frequent ← *Fracture appearances* → Less frequent

Readily formed

Figure 37 shows the spreading lengths together with the fracture positions marked as squares, circle, and triangles for the cases (SVT=1.8 Pa・s , CFST =1,000 Pa), (SVT = 1.8 Pa・s, CFST = 4,000 Pa), and (SVT = 1.8 Pa・s, CFST = 8,000 Pa). As shown in Figure 37, the number of calculated fractures tended to increase as the CFST was reduced. As discussed earlier in Table 3, the current best-estimate for the spreading profile of ECOKATS-V1 can be reproduced by two different combinations of SVT and CFST with crust fractures observed, namely, (SVT=1.8 Pa・s, CFST =4,000 Pa) and (SVT = 7.9 Pa・s, CFST = 4,000 Pa). The former combination describes a case in which crust is relatively readily formed and easily fractured than the latter combination. However, both cases seem to give too many crust fractures compared with the experimental observation, which indicates only a few fractures (Alsmeyer, et al., 2004). The discrepancy is due to the fact that the 2-D approximation requires "complete crust breach" into the plane of the 2-D geometry, whereas in reality, the initial crust fracture

develops from a "local weak spot." Due to the 2-D approximation, the current simulation results cannot give any quantitative evaluations for the solidification viscosity threshold or crust fracture stress. Such quantitative evaluations maybe for future study with 3-D analyses.
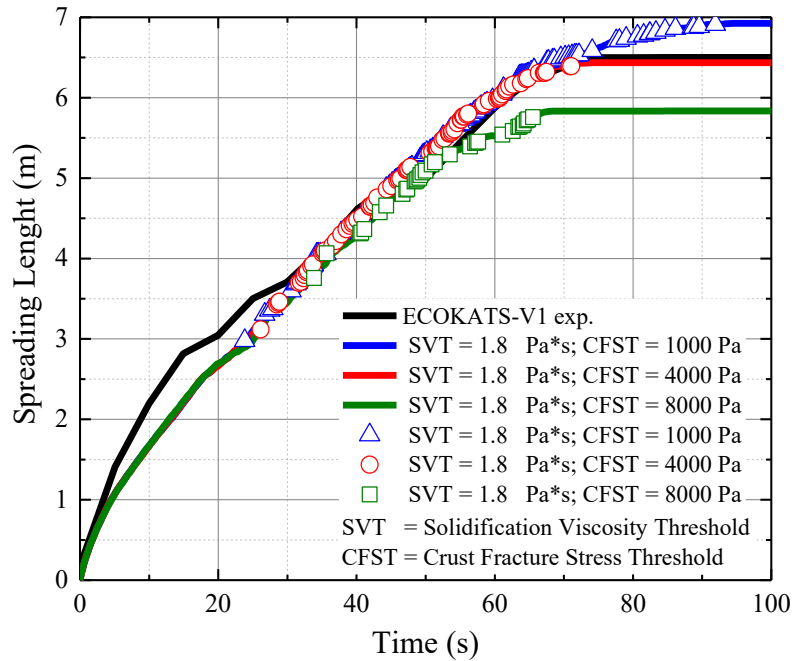
Figure 37 The spreading length (lines) and crust fracture appearances (symbols) for different CFST

The observed discrepancy between the MPS result and the experimental of the spreading profile from 1.0 m to 3.5 m (see *Figure 37*) could be explained due to several possible reasons. The first possible reason might be due to experimental uncertainty of the inlet mass flow rate which was not directly measured but derived from the linier approximation of thermit vessel mass deviation over the pouring time (Alsmeyer, et al., 2004). The second possible reason might be because of the overheated initial melt temperature (70K higher than its liquidus temperature) which may lead to no crust formation observed during the first 12s in the experiment (Alsmeyer, et al., 2004). In other words, during the first 12 s, the flow is considered to be isothermal-like spreading. In addition, the simulation condition could be another possible reason where in current simulation the thermal contact resistance on the melt-substrate interaction is neglected. This may result in over cooling of the leading edge which may slowdown the spreading distribution before the crust breakup occurred.

Figure 38 shows the time fraction of the timestep control by Courant number and Particle Number Density in the simulation cases with different SVTs and CFSTs. There seems a tendency for the time fraction of the timestep control by PND to decrease when the SVT and CFST increase. This indicates that locally particle-dense regions could have occurred more easily when applying a relatively small SVT and CFST. This is reasonable considering that a relatively small SVT and CFST can cause crust fractures to occur more easily and would increase the chances of sudden flow changes locally,

resulting in more operations of the necessary PND timestep control for the locally particle-dense regions.

Solidification Viscosity Threshold/Crust Fracture Stress Threshold
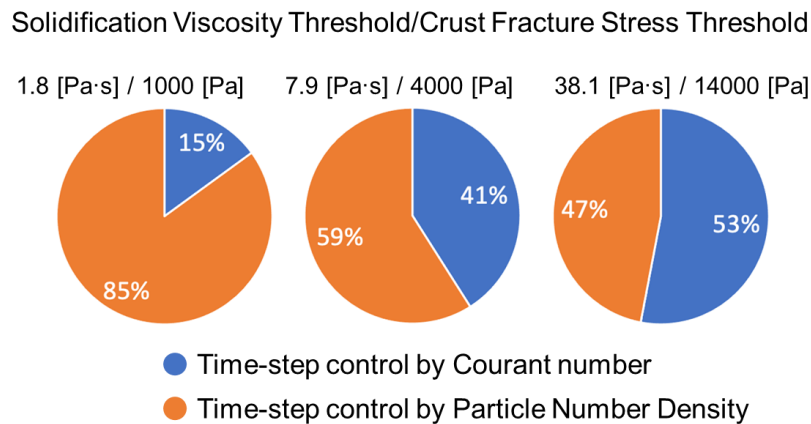
Figure 38 The time fraction of time-step control by Courant number and Particle Number Density in simulation cases with different SVTs and CFSTs

4.4. Discussions

In this chapter, the new timestep control for the MPS method has been developed, which is especially important when simulating melt spreading, which involves crust formation and fracture in low viscous dynamic flow. By implementing the newly developed timestep control, the developed MPS method can now be applied to a wide range of conditions, which involves crust formation and fractures with different formation and fracture thresholds. The key achievement of the developed analysis method can be highlighted, which still holds even if it is in 2-D, as follows:

Past studies: "Effects of" melt crust interactions at the leading edge were treated by artificially tuning the "bulk melt viscosity", which may result that the bulk melt viscosity may unrealistically be large in the simulations.

This study: Melt–crust interaction is relatively well modeled (mechanistically). Spreading termination of low viscous fluid by the leading-edge crust formation is considered. However, quantitative estimation of the spreading is beyond the scope of the current study, as the current simulations are limited to 2-D modeling due to computation cost.

As shown below in *Figure 39*, influence of sidewalls cannot be considered in 2-D. In reality, it is expected that the spreading is only terminated when crust anchoring takes place between the sidewalls, across the flow channel. Moreover, breach point in 3-D cannot be considered in 2-D, where breach is represented by breach line into the plane. Therefore, 3-D analysis is necessary for quantitative estimation of the spreading.

2D

Influence of sidewalls cannot be considered in 2-D

Breach point in 3-D cannot be considered in 2-D, where breach is represented by breach line into the plane.

3D
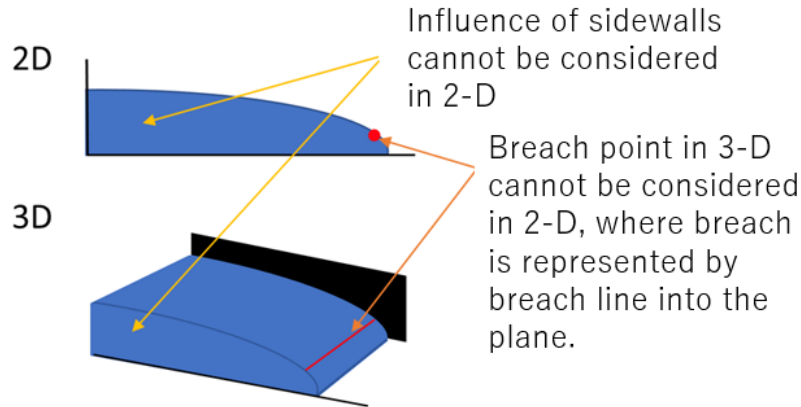
Figure 39 Breach point in 2-D vs 3-D simulation

The above-described discussions may be further elaborated as follows. Namely, the analyses with the improved MPS method show that the influence of the crust only becomes significant when it develops sufficiently at the leading edge so as to form a continuous crust layer from the top surface of the melt to the bottom base mat (i.e., so as to completely cover the leading edge with the crust layer). Otherwise, the crust seems to be simply floating on top of the melt and being carried with the bulk melt flow without imposing significant resistance to the bulk melt flow.

Such understanding may also be supported by the findings from the simulations of VULCANO VE-U7 (Chapter 3). That is, although the thermal contact resistance between the melt and the substrate had a significant influence on the interface crust development, it did not have important influences on the spreading profile of the melt. It may be understood that the cooling effect by the boundary wall only influences the interface melt temperature and solidification, but the influence does not extend to the bulk melt and the bulk melt continues to flow over the newly formed crust layer. In another word, the boundary wall cooling acts as if it is increasing the wall thickness (by incorporating the newly formed interface crust layer) while the melt thickness is being reduced (as the interface melt layer is being converted to a crust layer). The remaining bulk melt seems to simply flow over the newly formed crust layer without significant changes to the flow velocity profile.

Thus, it may be argued that the expected sidewall shear force and cooling effects are not large. However, as observed in the movie of the experiment, the sidewall plays an important role when the leading-edge crust develops across the flow channel and anchors between the two sidewalls. At this point, the spreading seems to fully terminate. Such mechanism cannot be modeled in the current 2-D analysis. Hence, for quantitative prediction of the ECOKATS-V1 experiment, 3-D analysis is necessary. Still, the improved MPS method in 2-D has demonstrated the key understanding of such phenomena. Namely, crust formation has limited influence on the melt spreading while it is freely flowing with the bulk melt or acting as a wall boundary. It only behaves as a resistance to the flow when the crust layer has sufficiently developed to cover the leading edge and bridge (anchor) to the wall boundary.

Lastly, it should be noted that the current "crust fracture" model of the developed MPS method still does not represent "mechanical fracture" accurately for quantitative discussions. This is partly due to the limitation of the calculation resolution. The crust film thickness may be much smaller than the particle size being used in the current MPS simulations (e.g., 2.0 mm). It means that the current MPS crust represents the crust film together with the melt in the vicinity of the crust film as a "smoothed (averaged) crust behavior". Then, it is obvious that the Crust Fracture Stress Threshold (CFST) defined in the thesis does not correspond to the real fracture stress of the crust and it is expected to be highly dependent on the particle size. With these understandings, the novelty of the current study is that, although with limited capability, this is the first time that melt spreading termination and restart (stop and go) has been modeled with respect to stress and strain acting on the leading edge (thereby incorporating the mechanical aspect of the melt spreading) rather than simply modeling with solidification and remelting of the past studies (limited to the thermal aspect of the melt spreading).

In summary, the followings may be important findings and discussion points:

(1) Crust does not a significantly influence the melt spreading while it is only floating on top of the melt or being formed by the wall boundary

(2) Crust does have significant influence on the melt spreading when it has sufficiently developed to cover the leading edge and bridge (anchor) the melt to the wall boundary

(3) Initiation of the crust fracturing (or possibly localized remelting) seems to involve random nature (from experiment movie), which challenges the deterministic simulation method

(4) The current MPS crust model treats the real crust and the melt in the vicinity of the crust as "averaged crust".

4.5. Conclusions

A new technique of timestep control has been developed in the MPS method, which has enabled simulations of melt spreading with crust formation and breach over a wide range of conditions, which may be encountered in the ECOKATS V1 spreading. The new timestep control with additional consideration of particle number density as a control parameter is confirmed to be effective for employing different crust formation and fracture threshold parameters, namely, Solidification Viscosity Threshold (SVT) and the Crust Fracture Stress Threshold (CFST) of the melt. The former determines the threshold viscosity above which the fluid is regarded as solid (crust). The latter determines the mechanical strength of the crust at the leading edge of the spreading front.

There still remain issues for future studies to further develop the method for more quantitative discussions. In particular, the current 2-D approximation requires "complete crust breach" into the plane of the 2-D geometry, whereas in reality, the initial crust fracture develops from a "local weak spot." Due to the 2-D approximation, the current simulation results cannot give any quantitative evaluations for the SVT or CFST. Such quantitative evaluations maybe for future study with 3-D analyses.

Chapter 5 Conclusions and Future Work

5.1. Conclusions

Despite the advantageous nature of the MPS method in modeling crust formation and melt – crust interactions in dynamic flow, the applicability of the MPS method had been limited due to lack of melt – substrate interaction model (contact heat resistance model) and lack of numerical stability when the crust is formed or breached in low viscous melt spreading. In this study, the new thermal contact resistance model and timestep control with an additional index parameter of particle number density have been developed. The two technological breakthroughs in MPS modeling have now opened new possibilities of the use of the improved MPS method to further deepen understanding of melt spreading. The analyses of VULCANO VE-U7 and ECOKATS-V1 have demonstrated such new frontiers for melt spreading analyses, which are crucial for assuring and improving the safety and reliability of nuclear power. The following conclusion can be drawn.

Accurate and numerically stable crust modeling in dynamic flow is the key requirement for deepening understanding of melt spreading for improving safety evaluations, accident managements, accident measures and designs of light water reactors under postulated severe accident conditions. Such crust modeling enables investigations into more detailed phenomena involved in melt spreading, such as melt – substrate interaction and influences of gas bubbles on melt spreading. The following new findings have been gained through analyses of VULCANO VE-U7 and ECOKATS-V1:

- Corium spreading is governed by melt – crust interaction, whose resistance to the flow only becomes significant when it has developed sufficiently at the leading-edge.
- Melt–substrate interaction does not have a direct influence on corium spreading, but decomposition gas bubbles from the concrete substrate may influence the bulk melt properties and the spreading when the spreading behavior is governed by the bulk melt property change. The bulk melt property change governs the spreading in VULCANO VE-U7, because of the wide solidification range (larger difference between the solidus and the liquidus temperatures). This is the fundamental reason for the difference observed between the ceramic and concrete channels of VULCANO VE-U7.
- The influences of the leading-edge crust formation and fracture are more evident for ECOKATS-V1 than for VULCANO VE-U7, because of much narrower solidification range of the melt. This is the fundamental reason of the "stop and go" behavior observed in ECOKATS-V1.
- For quantitative discussions, 3-D modeling is necessary to consider the crust anchoring and breaching.

5.2. Future work

While the current study has broadened new frontiers for deepening the understanding of melt spreading with the MPS method, the current MPS simulation capability is still limited primarily due to the high calculation cost. In this study, the crust is modeled with fluid particles with sufficiently large viscosity, so that it can be regarded as solid. This modeling is flexible and applicable to a wide range of flow patterns including cases, where the solidified crust is transported by bulk melt flow. However, the drawback is the large calculation cost associated with highly viscous fluid particles.

One way to reduce calculation cost may be to find a set of conditions, for which some of the heavy calculations can be skipped for solidified particles. Another way to reduce calculation cost is to apply variable particle sizes (resolutions) as often adopted with Eulerian mesh methods. However, it should be noted that both of these approaches require some nature of the Eulerian approach. Choices of such conditions for skipping calculations or boundaries to apply multi-resolution need to be carefully determined, so that the merit of Lagrangian method is not deteriorated. That is, the merit that the analyst does not need to know the flow pattern prior to the analysis. In another word, the analyst does not need to know where the particles may be transported to and at which location the particles may be converted to solid / liquid.

With the effort to reduce calculation cost, together with the effort to enhance parallelization efficiency, 3-D simulations of melt spreading may be possible not only for VULCANO VE-U7, but also for other experiments such as ECOKATS-V1. Then, the influences of crust anchoring across the sidewalls or propagation of crust breach from the fracture point may be discussed in more details. Moreover, multi-scale physics simulations involving solid, liquid, and gas (bubbles) may also be possible for experimental geometries.

Nomenclature

A	Surface area of the free-surface particles, (m^2)
B_μ	Bubble factor representing the viscosity-increase
C_i	Courant number of flow velocity
C_P	Specific heat capacity, (J/kg/K)
C_R	Empirical Ramacciotti parameter
$\mathbf{C}$	Corrective matrix
d	Dimension number
$\mathbf{f}$	External force (i.e., gravitational force, surface tension)
h	Specific enthalpy of the corium
h_0	Specific enthalpy of the corium at the solidus temperature
h_l	Specific enthalpy of the corium at the liquidus temperature
h_c	Thermal contact conductance (W/m²K)
i	Reference particle
j	Neighbor particles
k_{ij}	Effective heat conductivity, (W/m/K)
k_i	Heat conductivity of particle i
k_j	Heat conductivity of particle j
l_0	Diameter of particle size or Space between two adjacent particles (m)
l_i	Diameter of particle i, (m)
l_j	Diameter of particle j, (m)
m	Mass (Kg)
$\mathbf{n}$	Unit normal of free surface
n	Particle number density
n^0	Constant value of n
n_i^*	Particle number density of the i-th particle
$n_{condition}$	Threshold of particle number density
N	Number of neighbor particles
N^0	Constant value of N
N_i^*	Number of a neighbor particle of the i-th particle
P	Pressure, (Pa)
$\mathbf{P}$	Relative position vector
Q_e	Energy of radiation
R_c	Thermal contact resistance (m²K/W)

T	Temperature, (K)
T_m	Melting temperature (K)
T_{relax}	Relaxation time for historical memory, (s)
$\mathbf{r}_j$	Coordinate position of particle j
$\mathbf{r}_i$	Coordinate position of particle i
r_e	radius of interaction area (m)
$r = r_{ij}$	distance between particle i and particle j *(m)*
Δr_i	distance coefficient controlling the amplitude of position shifting (m)
t	Current moment, (s)
t'	Historical moment, (s)
Δt	Timestep, (s)
Δt_{lim}	Minimum timestep, (s)
$\mathbf{u}$	Velocity (m/s)
u_i	Maximum flow velocity of particle i
V	Volume (m^3)
w	weight function

Greek letters

λ	Initial particle distribution
β	Threshold parameters for the particle number density
β'	Threshold parameters for the number of neighbor particles
ε_A	Radiation emissivity by the free surface
$\varepsilon_{\alpha\beta}$	Strain rate tensor
γ	Solid fraction
μ	Dynamic viscosity, (Pa.s)
μ_{SVT}	Solidification viscosity threshold of the melt
μ_{liq}	Kinematic viscosity of the liquid phase
ρ	Density, (kg/m^3)
σ_{Stef}	Stefan-Boltzmann constant, ($W/m^2/K^4$)
σ_{Mises}	Von-Mises criterion
ϕ	Scalar variable

Abbreviation

CFST	Crust Fracture Stress Threshold
LWR	Light Water Reactor

MPS	Moving Particle Semi-implicit
OPS	Optimized Particle Shifting
PCV	Primary Containment Vessel
PND	Particle Number Density
PS	Particle Shifting
RPV	Reactor Pressure Vessel
SVT	Solidification Viscosity Threshold
MCCI	Molten Core-Concrete Interaction
EPR	European Pressurized-water Reactor
HVF	Highly Viscous Fluid

References

Allelein, H., Breest, A., & Spengler, C. (2000). Simulation of core melt spreading with LAVA: Theoretical background and status of validation. *Proceeding of the OECD workshop on ex-vessel debris coolability, IAEA, INIS.* Germany.

Alsmeyer, H., Cron, T., Foit, J., Messemer, G., Schmidt-Stiefer, S., Hafner, W., & Kriscio, H. (2004). *Test Report of the Melt Spreading Test ECOKATS-V1 and ECOCATS-1: Ex-Vessel core melt stabilization research.* Karlsruhe: ECOSTAR, Forschungszentrum Karlsruhe.

Chang, Y., Hou, T., Merriman, B., & Osher, S. (1996). A level set formulation of Eulerian interface capturing method for incompressible fluid flows. *Journal of Computational Physics, 124*, 449-464.

Cognet, G., Alsmeyer, H., Tromm, W., Magallon, D., Wittamaack, R., B.R.Sehgal, . . . Laffont, G. (2001). Corium spreading and coolability CSC Project. *Nuclear Engineering and Design, 209*, 127-138.

Dinh, T., Konovalikhin, M., & Sehgal, B. (2000). Core melt spreading on a reactor containment floor. *Progress in Nuclear Energy, 36*, 405-468.

Duan, G., Chen, B., Koshizuka, S., & Xiang, H. (2017). Stable multiphase moving particle semi-implicit method for incompressible interfacial flow. *Comput. Methods. Appl. Mech. Engrg, 318*, 636-666.

Duan, G., Koshizuka, S., & Yamaji, A. (2018a). An Accurate and Stable Multiphase Moving Particle Semi-Implicit Method Based on Corrective Matrix for All Particle Interaction Models. *Int. J. Numer. Math. Eng., 115*, 1287-1314.

Duan, G., Yamaji, A., & Koshizuka, S. (2018b). A Novel Approach for Crust Behaviors in Corium Spreading Based on Multiphase MPS Method. Qingdao - China: Proceeding of 12th International Topical Meeting on Nuclear Reactor Thermal-Hydraulic, Operation and Safety.

Duan, G., Yamaji, A., & Koshizuka, S. (2019). A novel multiphase MPS algorithm for modeling crust formation by highly viscous fluid for simulating corium spreading. *Nuclear Engineering and Design, 343*, 218-231.

Eigel, G., Fieg, G., Massier, H., Stegmaier, U., & Schutz, W. (2000). *KATS experiments to simulate corium spreading in the EPR core catcher concept.* Wissenschaftliche Berichte FZKA 6475, 148-155.

Eppinger, B., Fieg, G., Schutz, W., & Stegmaier, U. (2001). KATS Experiments to Simulate Corium Spreading in the EPR Core Catcher Concept. *International conference on nuclear engineering.* France.

Farmer, M. (2009). *Melt Spreading Code Assessement, Modifications, and Applications to the EPR Core Catcher Design.* Chicago: Nuclear Engineering Division, Argonne National Laboratory.

Fischer, M. (2004). The severe accident mitigation concept and the design measures for core melt retention of the European Pressurized Reactor (EPR). *Nuclear Engineering and Design, 230*, 169-180.

Foit, J. (2002). Spreading on ceramic and concrete substrate in KATS experiments. *Proc. Annu. Meeting Nucl. Technol.*

Foit, J. (2006). Large-scale ECOKATS experiments: Spreading of oxide melt on ceramic and concrete surfaces. *Nuclear Engineering and Design, 236*, 2567-2573.

Hirt, C., & Nichols, B. (1981). Volume of fluid (VOF) method for the dynamics of free boundaries. *J. Comput. Phys., 39*, 201-225.

Journeau, C., Boccaccio, E., Brayer, C., Cognet, G., Haquet, J., Jegou, C., . . . Monerris, J. (2003). Ex-vessel corium spreading: result from VULCANO Spreading tests. *Nuclear Engineering and Design, 223*, 75-102.

Journeau, C., Haquet, J., Spindler, B., Spengler, C., & Foit, J. (2006). The VULCANO VE-U7 Corium spreading benchmark. *Progress in Nuclear Energy 48, 48*, 215-234.

Kawahara, T., & Oka, Y. (2012). Ex-vessel molten core solidification behavior by moving particle semi-implicit method. *Journal of Nuclear Science and Technology, 49*(12), 1156-1164, DOI: 10.1080/00223131.2012.740944.

Kays, W. M. (1994). Turbulent Prandtl Number - Where are We? *Journal of Heat Transfer, 116*((2)),

284-294.

Khayyer, A., Gotoh, H., & Shimizu, Y. (2017). Comparative study on accuracy and conservation properties of two particle regularization shcemes and proposal of an optimized particle shifting scheme in ISPH context. *Journal of Computational Physics, 332*, 236-256.

Koshizuka, S., & Oka, Y. (1996). Moving Particle Semi-Implicit Method for Fragmentation of Incompressible Fluid. *Nuclear Science and Engineering, 123*, 421-434.

Li, G. (2015). *Study on Melt Behavior in a BWR Lower Head by MPS Method and MELCOR Code.* Waseda University. Retrieved from http://hdl.handle.net/2065/45708

Mader, H., Llewellin, E., & Mueller, S. (2013). The rheology of two-phase magmas; A review and analysis. *Jounal of Volcanology and Geothermal Research, 257*, 135-158.

Manga, M., & Loewenberg, M. (2001). Viscosity of magmas containing highly deformable bubles. *Journal of Volcanology and Geothermal Research, 105*, 19-24.

Masumura, D., Oka, Y., Yamaji, A., & Furuya, M. (2015). Analysis of metal vessel wall ablation experiment with high temperature liquid by MPS method. *16th International Topical Meeting on Nuclear Reactor Thermal Hydraulics 2015. 9*, pp. 7401-7413. Chicago, United States: American Nuclear Society.

Matsuura, T., & Oka, Y. (2013). MPS simulation of spreading behaviour of molten materials. *International Conference on Particle-based Methods-Fundamentals and Applications Particles.* Stuttgart.

Ramacciotti, M., Journeau, C., Sudreau, F., & Cognet, G. (2001). Viscosisty models for corium melts. *Nuclear Engineering and Design, 204*, 377-389.

Spengler, C. (2004). Simulation of Melt Spreading in Consideration of Phase Transitions. *EUROSAFE Forum, IAEA, INIS.* Germany.

Spindler, B., & Veteau, J. (1998). Status of the Assessment of the Spreading Code THEMA Againts the Corine Experiments. *JAERI Conf.* Framce.

Spindler, B., & Veteau, J. (2004). Simulation of spreading wiht solidification: assessment synthesis of THEMA code. *IAEA, INIS, CEA Saclay.* France.

Spindler, B., & Veteau, J. (2006). The simulation of melt spreading with THEMA code Part 1: Model, assessment strategy and assesment againts analytical and nimerical solution. *Nuclear Engineering and Design , 236*, 415-424.

Spindler, B., Vetau, J., Cecco, L. d., Montanelli, P., & Pineau, D. (2000). Assessment of THEMA code againts spreding experiments . *IAES, INIS.* Germany.

Steinwarz, W., Alemberti, A., Hafner, W., Alkan, Z., & Fischer, M. (2001). Investigation on the phenomenology of ex-vessel core melt behavior (COMAS). *Nuclear Engineering and Design, 209*, 139-146.

Takahashi, N., Duan, G., Furuya, M., & Yamaji, A. (2019). Analysis of hemispherical vessel ablation failure involving natural convection by MPS method with corrective matrix. *International Journal of Advanced Nuclear Reactor Design and Technology, 1*, 19-29.

Tamai, T., & Koshizuka, S. (2014). Least squares moving particle semi-implicit method - An arbitrary high order accurate meshfree Lagrangian approach for incompressible flow with free surface. *Comp. Part. Mech., 1*, 277-305.

Tanaka, M., & Masunaga, T. (2010). Stabilization and smoothing of pressure in MPS method by quasi-compressibility. *Journal of Computational Physics, 229*, 4279-4290.

Theofanous, T., Yan, H., Podowski, M., Cho, C., Powers, D., Heames, T., . . . Powers, D. (1993). *The probability of Mark-I containment failure by melt-attact of the liner.* Washington DC: Division of Systems Research, Office of Nuclear Regulatory Research, U.S. Nuclear Regulatory Commission.

Tromm, W., & Foit, J. (1999). Dry and wet spreading experiment with prototypical material at the FARO facility and thoretical analysis. OECD Workhsop on Ex-Vessel Debris Coolability, Karlsruhe, Germany, 15-18 November 1999: Forschungszentrum Karlsruhe (FZK), GmbH.

Tromm, W., Foit, J., & Magallon, D. (2000). Dry and wet spreading experiment with prototypic material at the FARO facility and theoretical analysis. *Proceedings of the OECD workshop on ex-vessel debris coolability.* Germany.

Uchida, K., Duan, G., & Yamaji, A. (2018). Numerical Investigation of the stop-and-go mechanism in

FARO L26S spreading experiment by MPS method. *12th International Topical Meeting on Nuclear Reactor Thermal-Hydraulics, Operation and Safety (NUTHOS-12)*. Qingdaou, China.

Unverdi, S., & Tryggvason, G. (1992). A front-tracking method for viscous, incompressible multi-fluid flows. *Journal of Computational Physics, 100*, 25-37.

Wittmaack, R. (1997). CORFLOW: a code for the numerical simulation of free-surface flow. *Nucl. Technol, 119*, 159-180.

Xu, R., Stansby, P., & Laurence, D. (2009). Accuracy and stability in incompressible SPH (ISPH) based on the projection method and a new approach. *Journal of Cmputational Physics, 228*, 6703-6725.

Yasumura, Y., Yamaji, A., Furuya, M., Ohishi, Y., & Duan, G. (2017). Investigation on influence of crust formation on VULCANO VE-U7 corium spreading with MPS method. *Annals of Nuclear Energy, 107*, 119-127.

Ye, I.-S., Kim, J. A., Ryu, C., Ha, K. S., Kim, H. Y., & Song, J. (2013). Numerical investigation of the spreading and heat transfer characteristics of ex-vessel core melt. *Nuclear Engineering and Technology, 45*(1), 21-28.

早稲田大学　博士（工学）　学位申請　研究業績書

(List of research achievements for application of doctorate (Dr. of Engineering), Waseda University)

氏　名　Jubaidah　　　　　　　　　　　　　　印(seal or signature　　　　　　　　)

（As of 6th May, 2021）

種 類 別 (By Type)	題名、　　発表・発行掲載誌名、　　発表・発行年月、　　連名者（申請者含む）(theme, journal name, date & year of publication, name of authors inc. yourself)
(1) Paper 　○ 　○	1. **Jubaidah**, G. Duan, A. Yamaji, C. Journeau, L. Buffe, J.F. Haquet, "Investigation on Corium Spreading Over Ceramic and Concrete Substrates in VULCANO VE-U7 Experiment with Moving Particle Semi-Implicit Method", *Annals of Nuclear Energy 107266*, Vol. 141, January (2020). 2. **Jubaidah,** Y. Umazume, N. Takahashi, X. Li, G. Duan, A. Yamaji, "2D MPS Method Analysis of ECOKATS-V1 Spreading with Crust Fracture Model", *Nuclear Engineering and Design,* 379(2021)111244.
(2) Presen-tation	1. **Jubaidah**, A. Yamaji, "Investigation on Influence of Thermal Resistance on Corium Spreading over Ceramic Substrate with MPS Method", The Symposium of the Nuclear Safety Seismic Design, Tokyo City University, December 1, 2017, Tokyo – Japan (2018). 2. **Jubaidah**, G. Duan, and A. Yamaji, "Sensitivity Analysis of VULCANO VE-U7 Corium Spreading with MPS Method", 11 AESJ Student Conference, March 1, 2018, Tokyo – Japan (2018). 3. **Jubaidah**, G. Duan, A. Yamaji, "Numerical Investigation on VULCANO VE-U7 Corium Spreading over Ceramic/Concrete with MPS Method", The 12th International Topical Meeting on Nuclear Reactor Thermal-Hydraulic, Operation and Safety (NUTHOS-12), October 14 – 18, 2018, Qingdao – China (2018). 4. **Jubaidah**, G. Duan, A. Yamaji, "MPS-THEMA Crosswalk: Additional Result on Phase-1 with MPS Method since the 2nd Workshop and Discussion on Comparison with THEMA", April 22 – 24, 2019, Tokyo – Japan (2019). 5. **Jubaidah**, G. Duan, A. Yamaji, "MPS-THEMA Crosswalk: Specification on Phase-2 and Preliminary Results with MPS Method", April 22 – 24, 2019 Tokyo – Japan (2019). 6. **Jubaidah**, G. Duan, A. Yamaji, "Analysis of VULCANO VE-U7 Ceramic and Concrete Double Channel Configuration with MPS Method", July 10 -12, 2019, Fukushima – Japan (2019).